remote sensing

MDPI

Article

The Influence of Reservoirs on Landslide Erosion

Fengjiao Tang [1,2], Shengwen Qi [1,2,3], Songfeng Guo [1,2,*], Yongchao Li [1,2], Xinyi Guo [1,2], Xiao Lu [1,2], Yu Zou [1,2,3], Xueliang Wang [1,2,3], Xie Hu [4], Lina Ma [1,2], Bowen Zheng [1,2] and Zan Wang [1,2]

[1] State Key Laboratory of Lithospheric and Environmental Coevolution, Institute of Geology and Geophysics, Chinese Academy of Sciences, Beijing 100029, China; tangfengjiao@mail.iggcas.ac.cn (F.T.); qishengwen@mail.iggcas.ac.cn (S.Q.); liyongchao@mail.iggcas.ac.cn (Y.L.); guoxinyi@mail.iggcas.ac.cn (X.G.); luxiao@mail.iggcas.ac.cn (X.L.); zouyu@mail.iggcas.ac.cn (Y.Z.); wangxueliang@mail.iggcas.ac.cn (X.W.); malina@mail.iggcas.ac.cn (L.M.); zhengbowen@mail.iggcas.ac.cn (B.Z.); zan.wang@mail.iggcas.ac.cn (Z.W.)
[2] University of Chinese Academy of Sciences, Beijing 100049, China
[3] China-Pakistan Joint Research Center on Earth Sciences, CAS-HEC, Islamabad 45320, Pakistan
[4] College of Urban and Environmental Sciences, Peking University, Beijing 100871, China; hu.xie@pku.edu.cn
* Correspondence: guosongfeng@mail.iggcas.ac.cn

Abstract: The evolution of the landslide erosion of bank slopes in reservoir regions is crucial for disaster prevention and mitigation in hydropower projects, and it is also an important topic to investigate the impact of anthropogenic activities on the environment. A dispute exists on the landslide erosion of bank slopes under reservoir impoundment. In this paper, we chose the Xiluodu reservoir as a typical case for analysis. The reservoir is located on the eastern Qinghai–Tibetan Plateau and ranks as the fourth largest hydropower station in the world. Firstly, we identified landslides using the multi-temporal image interpretation method before and after impoundment in the reservoir area, and established a landslide dataset. On this basis, we analyzed the spatiotemporal distribution of these landslides, and derived the landslide erosion rate based on the quantitative relation between landslide volume and area. The results showed that the landslide erosion rate increased sharply during the initial impoundment period and decreased exponentially. We then analyzed reservoir-induced landslides worldwide and found that most reservoir bank slopes tend to stabilize after about five years of impoundment, eventually even becoming more stable than pre-impoundment, regardless of the location, scale, water fluctuations, and geoenvironment. Thus, in the long term, reservoir construction tends to reduce erosion and contribute to bank stability. This study provides a preliminary answer to the controversial issue of the impact of reservoir construction on the natural environment.

Keywords: reservoir impoundment; landslide erosion; spatiotemporal distribution; long-term evolution trend

Academic Editors: Constantine A. Stamatopoulos, Baofeng Di, Angelos Protopapas and Giordano Teza

Received: 25 December 2024
Revised: 5 February 2025
Accepted: 6 February 2025
Published: 7 February 2025

Citation: Tang, F.; Qi, S.; Guo, S.; Li, Y.; Guo, X.; Lu, X.; Zou, Y.; Wang, X.; Hu, X.; Ma, L.; et al. The Influence of Reservoirs on Landslide Erosion. *Remote Sens.* **2025**, *17*, 569. https://doi.org/10.3390/rs17040569

1. Introduction

Landslide erosion refers to a process in which part of the rock and soil mass on a slope undergoes failure along a defined rupture surface under the influence of gravity, slides downward and forward, and accumulates at a relatively short distance [1]. The initial rising and subsequent fluctuation of reservoir water can cause significant changes in hydrological conditions in the surrounding geological body, and lead to intensified landslide erosion in the reservoir area. For example, more than 500 landslides occurred on the

bank slopes of Roosevelt Lake during the 12-year reservoir operation from 1941 to 1953, causing severe economic losses [2,3]. A catastrophic bank slope failure occurred in Vajont Reservoir after 4 years of operation in 1963, resulting in more than 2600 casualties [4]. Since the Three Gorges Reservoir began to impound in 2003, 4429 geohazardous events have occurred [5], among which the Qianjiangping landslide occurred soon after the initial impoundment and generated a 30 m high impulse wave, resulting in 24 lives lost and 346 buildings damaged [6]. Typical reservoir-induced landslides have been studied to clarify how reservoir impounding can induce instability of the bank slope. Field monitoring and investigations have shown that the development of a reservoir landslide is not just an instantaneous event, but always a long-term progressive process from deformation initiation to eventual failure along with damage accumulation and strength degradation [4,7–11]. Reservoir inundation, water fluctuations, and rainfall are the main factors that promote this long-term progressive process [8,12–14]. This long-term progressive process may exhibit different deformation and stability patterns due to varying internal and external conditions. Some landslides may accelerate and fail, while others may slow down and reach a stable state. For example, the Vajont landslide in Italy experienced a sudden failure in 1963 after creeping for three years, accumulating nearly 4 m of displacement before the disaster occurred [15]. In contrast, the Central Landslide in northern Poland showed increased activity during three different periods after the initial filling of the Włocławek reservoir in the early 1970s. However, no movement has been recorded within the landslide since March 2011 [16]. Existing studies have also found that some reactivated landslide masses begin to undergo a self-stabilizing process (the self-stabilizing process of a landslide refers to the promotion of slope stability through the self-regulation of factors such as the physical properties of the soil, geometric configuration, and other related parameters following the initial displacement of the landslide mass) as displacement accumulates [15,17]. But the mechanism of this self-stabilizing process remains unclear. Understanding the long-term evolutionary trends and mechanism of landslides after reactivation remains worthy of considerable attention.

Some scholars have researched periods of frequent landslide incidence after reservoir impoundment from a statistical perspective. For example, Jones [2] noted that nearly half of landslides in the Roosevelt Lake developed during the initial reservoir impoundment period in 1941–1942. Li [18] disclosed that the landslides at the Huanglongtan Reservoir exhibited a concentrated outbreak of over 20 landslides within the first two years after impoundment. Riemer [19] concluded that 85% of landslides reactivated either during reservoir construction or within the first two years after impoundment based on the data from 60 published cases. In the Three Gorges Reservoir, many landslides reactivated during the initial water rise to the normal level [20,21]. The above findings indicate that the reservoir impounding stage is a key triggering period for reservoir-induced landslides, as shown by statistical counting of the number of landslides. Yet, the evolution of reservoir-induced landslides with an increasing duration of reservoir impoundment is still not fully understood.

In recent years, 149 large-scale hydropower stations have been operated along the rivers in the Hengduan Mountain of the eastern Qinghai–Tibetan Plateau [22]. The region characterizes intense endogenic and exogenic geological processes, resulting in a landslide-prone geological environment. There is always a dispute on whether the impact of reservoir construction on the geological environment is positive or negative, especially in such an active orogenic belt.

The establishment of a multi-temporal landslide inventory is crucial for studying the evolution of reservoir-induced landslide erosion. Many approaches can be used to create a multi-temporal landslide inventory map. The traditional method is field geological surveys [18,21]. However, this is no longer economically viable for widespread areas, and

some long-term field survey information is not easily accessible. Optical remote sensing enables the multi-temporal interpretation of landslides over large areas. For instance, Behling et al. [23] utilized multi-sensor optical remote sensing imagery to create multi-temporal landslide inventory maps in southern Kyrgyzstan. Although manual visual interpretation is time-consuming and labor-intensive, it remains a reliable method for obtaining accurate landslide data [24,25]. Significantly, the advent in 2005 of Google Earth®, which offers multi-temporal imagery with a maximum resolution of up to 0.6 m, and the ability to look at the images in 3D, has greatly improved the efficiency of visual interpretation [26]. Ground-based radar and LiDAR have evolved in the last few decades [27], enabling the creation of high-resolution and precise digital elevation models [28]. The main difficulty is acquiring historical data with adequate spatial resolution to detect ground movements, without relying on ground-based measurements [13]. Interferometric Synthetic Aperture Radar (InSAR) is one of the most advanced tools for monitoring long-term ground deformation. It has the advantages of wide spatial coverage and the capability for constant operation in all weather conditions. Previous studies have carried out regional landslide mapping [29–31], landslide displacement monitoring [32,33], and landslide mechanism analysis [13,34] using InSAR. However, the establishment of a multi-temporal landslide inventory in areas characterized by a humid climate, dense vegetation, and steep terrain faces challenges such as poor image continuity, geometrical distortions, temporal and volume decorrelation, and severe atmosphere artifacts [35]. In summary, for the establishment of a multi-temporal landslide inventory in mountainous canyon areas, manual visual interpretation based on optical remote sensing remains the most reliable and feasible method. Building on this, this study established a database incorporating 536 landslides within the Xiluodu reservoir area along the Jinsha River on the eastern Qinghai–Tibetan Plateau. Through multi-temporal satellite image analysis and field surveys, we identified the occurrence time of these landslides from 2010 to 2023, covering both the pre- and post-reservoir impoundment stages. Then, the landslide erosion rate of the reservoir banks was calculated using the empirical relationship between landslide volume and area. We compared the spatiotemporal distribution of landslides before and after reservoir impoundment. Combined with two long-term deformation monitoring cases of reservoir-induced landslides and 63 published regional cases, we clarified the evolutionary trend of bank slope stability in the Xiluodu reservoir area. (Slope stability is typically assessed using the safety factor (FS) [36], which is the ratio of the resisting forces to the driving forces. When $FS > 1$, the slope is considered stable; when $FS = 1$, the slope is in a state of critical equilibrium; and when $FS < 1$, the slope is unstable.) Finally, we discussed the long-term effects of reservoirs on the geoenvironment.

2. Geological Settings of the Study Area

The study area is located in SW China, on the eastern margin of the Qinghai–Tibetan Plateau (Figure 1a). Generally, from NW to SE, the elevation decreases gradually from 5000 to 1000 m. Tectonically, the area belongs to the Daliangshan sub-block, which is adjacent to the Sichuan–Yunnan Rhombic Block. Several famous strike–slip faults have developed in these blocks; they are the Jiali–Nujiang fault (JL–NJF), Lan Cang Jiang fault (LCJF), Jinsha fault (JSF), Litang–Dewu fault (LT–DWF), Xianshuihe fault (XSHF), Anninghe fault (ANHF), and Xiaojiang fault (XJF), from W to E (Figure 1a). Overall, they strike N–S or NW–SE, which controls the rivers direction as well. Rivers continuously create incision-formed deep valleys and huge mountains in this region, which is composed of a unique geographical unit named the Hengduan Mountain region in China.

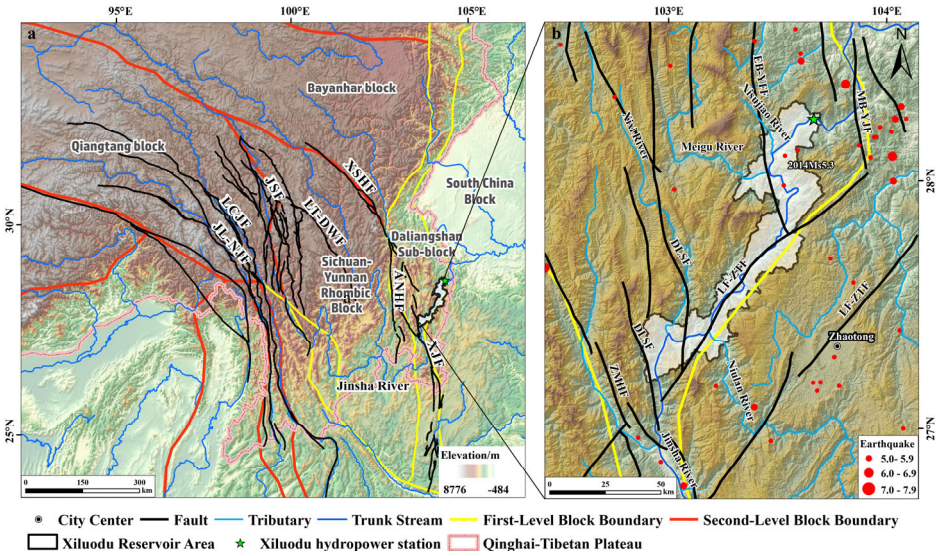

Figure 1. (**a**) The regional structure (the boundary data of the blocks refer to Zhang et al. [37] and fault data (1:4,000,000) from Qi [38]). JL–NJF: Jiali–Nujiang fault; LCJF: Lan Cang Jiang fault; JSF: Jinsha fault; LT–DWF: Litang–Dewu fault; XSHF: Xianshuihe fault; ANHF: Anninghe fault; XJF: Xiaojiang fault. (**b**) Faults and earthquakes (data from http://data.earthquake.cn, accessed on 30 January 2025) in the Xiluodu reservoir area. ZMHF: Zemuhe fault; DLSF: Daliangshan fault; EB–YFF: Erbian–Yanfeng fault; MB–YJF: Mabian–Yanjin fault (MB–YJF); LF–ZTF: Lianfeng–Zhaotong fault.

The Xiluodu Hydropower Station is located downstream of Jinsha River (Figure 2a). It has a double-curvature arch dam with a maximum height of 285.5 m. The installed capacity reaches 13,860 MW and ranks as the fourth largest globally, following the Three Gorges, Baihetan, and Yatapi Hydropower Stations. The reservoir has a normal pool level of 600 m and a total storage capacity of 1.27×10^{10} m^3, with a length of 195.1 km and an area of 133.65 km^2 for the reservoir at its normal level.

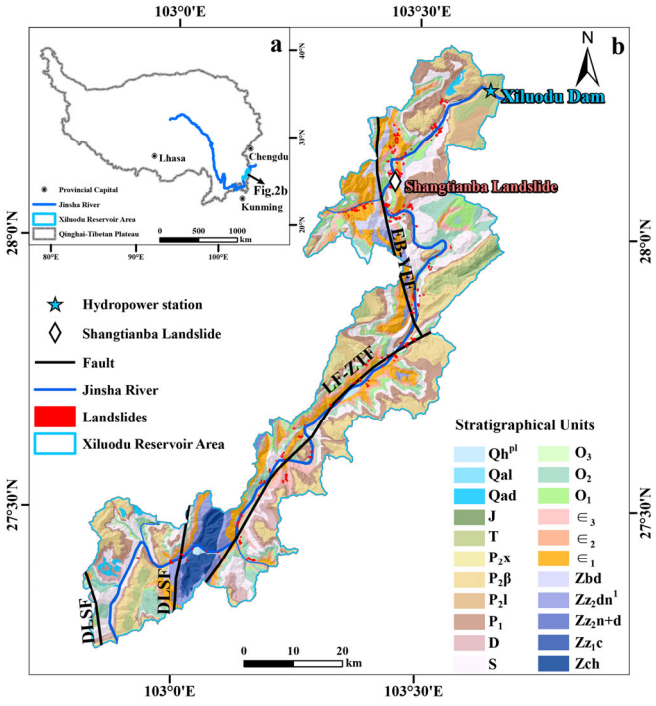

Figure 2. (**a**) A map of the Qinghai–Tibetan Plateau; (**b**) the geographic location, lithology [39], and landslide distribution of the reservoir area. See Table S1 for the meanings of the abbreviations for the stratigraphic units.

In the study area, except for the Carboniferous and Tertiary strata, the stratum ranging from the Precambrian to the Quaternary are all exposed (Figure 2b). Shale, primarily deposited in the Silurian (S) and Ordovician (O) strata, is the most widely distributed and covers 37.40% of the study area. Carbonate rock is the second most widespread, covering 27.08% (Table S1). It includes limestone and dolomite of the Upper Permian formation (P_1), the Lower Cambrian formation ($\in_3$), and the Sinian system Dengying formation (Zz_2dn^1, Zbd). And the Sinian system Dengying formation (Zz_2dn^1, Zbd) is distributed on both sides of the Daliangshan Fault Zone (DLSF), Erbian–Yanfeng Fault Zone (EB–YFF), and Lianfeng–Zhaotong Fault Zone (LF–ZTF) (Figure 2b), resulting in a relatively fragmented state. Upper Permian Emeishan basalt ($P_2\beta$) accounts for 16.5% of the reservoir area; it is the main stratum exposed in the dam area and the near-dam reservoir section (Figure 2b). Quaternary loose deposits account for the smallest area proportion and are mainly located in outcrops on the left bank of the dam site area and the tail section of the reservoir.

The tectonics system in the reservoir area is composed of several NNW-trending faults, including the Mabian–Yanjin Fault Zone (MB–YJF), Zemuhe Fault Zone (ZMHF), DLSF, and EB–YFF (Figure 1b). MB–YJF exhibits characteristics of left-lateral strike–slip and compressional thrusting activities in the late Quaternary. The other fault zones are predominantly characterized by left-lateral strike–slip movements. The NE-trending LF–ZTF is primarily dominated by compressional activities along with some dextral activity [40]. Most major earthquakes ($Ms \geq 6.0$) occur along the MB–YJF (Figure 1b). The reservoir area is stable with few earthquakes occurring throughout history, but experienced intensive microseismicities after reservoir impoundment on 4 May 2013, with the strongest earthquake of Ms 5.3 occurring in 2014 within the reservoir area [41].

The Xiluodu reservoir has a well-developed river system with many tributaries. The Niulan River flows in from the right bank, while the Xisujiao, Meigu, and Xixi Rivers flowing in from the left bank (Figure 1b). The topography of the reservoir area is influenced by the distribution of these rivers. We divided the slope gradient of the Xiluodu reservoir area into eight categories with an interval of 10° (Figure S1). The regions with slope gradients above 60° are mostly distributed along rivers, indicating that the river erosion has formed steep, deeply cut valley landforms. The categories of 10–20°, 20–30°, and 30–40° all cover more than 20% of the study area, and the categories of 60–70° and 70–80° cover less than 1% of the study area. The category of 0–10° is mainly distributed at higher elevations, indicating the development of high-altitude, low-relief terrain in the study area, which is most widely distributed close to the dam.

The reservoir area possesses a typical subtropical climate. The rainy season is from May to October, accounting for 85% to 90% of the total annual precipitation, with an especially high possibility of heavy rainfall from June to August [42], as shown in Figure 3. The reservoir underwent two significant impoundments during the rainy season. The first occurred from May 2013 to November 2013, with the water level rising from 420 m to 560 m. The second event was from June 2014 to September 2014, with the water level increasing from 540 m to 600 m. The reservoir level fluctuated between 540 m and 600 m in the following years (Figure 3).

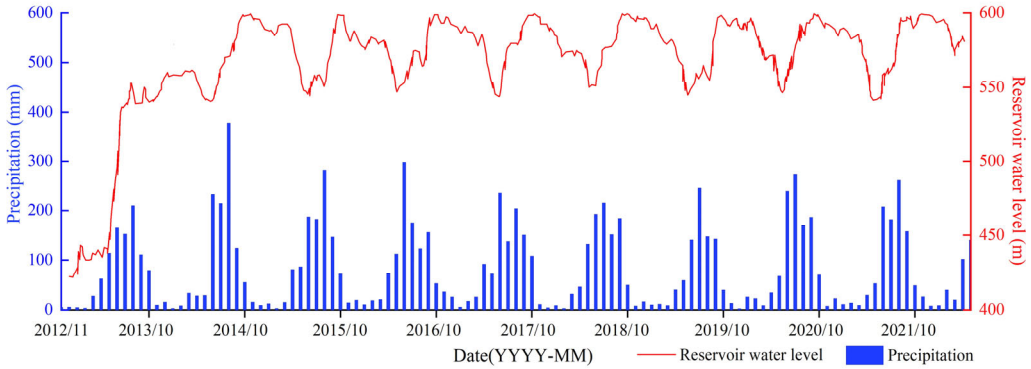

Figure 3. Water level and rainfall [42] variations in the Xiluodu reservoir area.

3. Data and Methodology

3.1. Interpretation of Multi-Temporal Landslides in the Reservoir Area

We chose the visual interpretation method based on multi-temporal optical images in Google Earth® to establish the multi-temporal landslide database. Other advanced technologies such as InSAR and LiDAR have significant limitations that made them unsuitable for this work. InSAR is good for large-scale landslides with long-term slow deformation [43,44]. However, it is less effective in identifying small reservoir-induced landslides with rapid deformation. And no SAR data were available for the most critical period (2010.10–2014.10) for landslide identification in the Xiluodu reservoir area [44]. LiDAR data from both before and after impoundment are difficult to acquire. Google Earth® can effectively offer multi-temporal imagery from 2010 to 2023, which makes it an effective tool to identify landslides before and after reservoir impoundment.

The steps for establishing a multi-temporal landslide database are as follows:

(1) Define the interpretation range. This study defines the interpretation range as the side slope between the pre-impoundment river surface (elevation 420 m) and the first watershed ridge line on both sides. We utilized ArcGIS hydrological analysis tools to process the ASTER GDEM 30 m resolution elevation data, extracting the watershed of the study area, as shown by the black boundary in Figure 1. The DEM data were obtained from the Geospatial Data Cloud site, Computer Network Information Center, Chinese Academy of Sciences (http://www.gscloud.cn, accessed on 30 January 2025), and the preprocessing work was also performed using this website.

(2) Preprocess optical images. We used Google Earth imagery and Sentinel-2 satellite imagery for joint interpretation. Table 1 shows the remote sensing images we used before and after impoundment. Google Earth imagery requires no preprocessing, and the data originate from the QuickBird and SPOT5 satellites. Sentinel-2 images were downloaded from https://dataspace.copernicus.eu/ (accessed on 30 January 2025), which had undergone radiometric calibration and atmospheric correction. Therefore, we directly resampled the images using SNAP 11 software, imported them into ENVI for band fusion, and finally exported them as TIFF files to be imported into ArcGIS for interpretation. Google Earth provides images with the best observation conditions each year (Table 1), and we complemented this with Sentinel-2 satellite images taken in clear, cloudless weather (Table 1), ensuring that at least one image from each source was available annually. To ensure consistency in data interpretation standards, the initial interpretation in 2021, as well as the verification and supplementation in 2022 and 2023, were all conducted by the same person.

Table 1. Remote sensing data used in this study.

Data Type	Data Sources	Data Acquisition Time	Spatial Resolution (m)
Pre-impoundment data	Google Earth images	2010/2/8, 2010/4/5, 2011/12/6, 2012/11/14, 2013/3/14	0.5–1
After-impoundment data	Google Earth images	2013/5/21, 2013/11/6, 2014/4/30, 2015/1/23, 2015/3/8, 2016/7/20, 2017/8/27, 2017/4/19, 2018/1/24, 2018/3/3, 2019/4/19, 2020/2/5, 2020/3/8, 2020/3/26, 2020/4/8, 2021/3/12, 2022/11/8, 2023/1/11, 2023/2/14, 2023/3/14	0.5–1
	Sentinel-2 images [1]	2015/12/27, 2016/5/5, 2017/2/19, 2018/3/3, 2018/4/2, 2019/4/7, 2020/1/12, 2020/11/17, 2020/12/27, 2021/3/27, 2022/1/1, 2022/11/27, 2023/1/6, 2023/1/29	10

[1] Sentinel-2 images are from https://glovis.usgs.gov/ accessed on 30 January 2025.

(3) Landslide interpretation. The interpretation of reservoir-induced landslides primarily relies on the distinct tonal differences in the images, where the landslide area appears grayish-white compared to the surrounding environment. The landslide surface is almost devoid of vegetation, with significant surface damage, exposed soil, rough texture, and an irregular boundary. And we also compared the images before and after impoundment to determine the distribution of reservoir-induced landslides. We determined the point at which the landslide first appeared in the images as the occurrence time for reservoir-induced landslides. Some of the reservoir-induced landslides expanded continuously after the original generation. For such landslides, we considered every expansion as one separate landslide and determined the occurrence time according to the corresponding expansion time. Taking the Shangtianba landslide as an example (the location is shown in Figure 2b), the slope had no signs of deformation before impoundment (Figure 4a), and an original landslide initiated in 2014 (Figure 4b), followed by two expansions in 2015 and 2017 (Figure 4c,d). The two expansions were delineated as landslides occurring in 2015 and 2017, respectively. Finally, we identified a total of 54 landslides from February 2010 to March 2013 and 482 reservoir-induced landslides from May 2013 to January 2023 in the Xiluodu reservoir area before and after impoundment, as illustrated in Figure 2b.

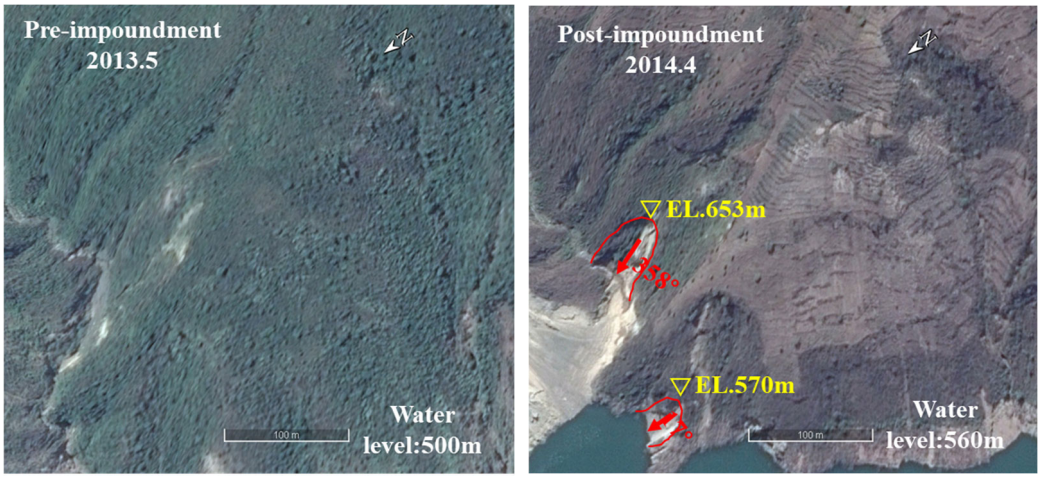

(**a**) (**b**)

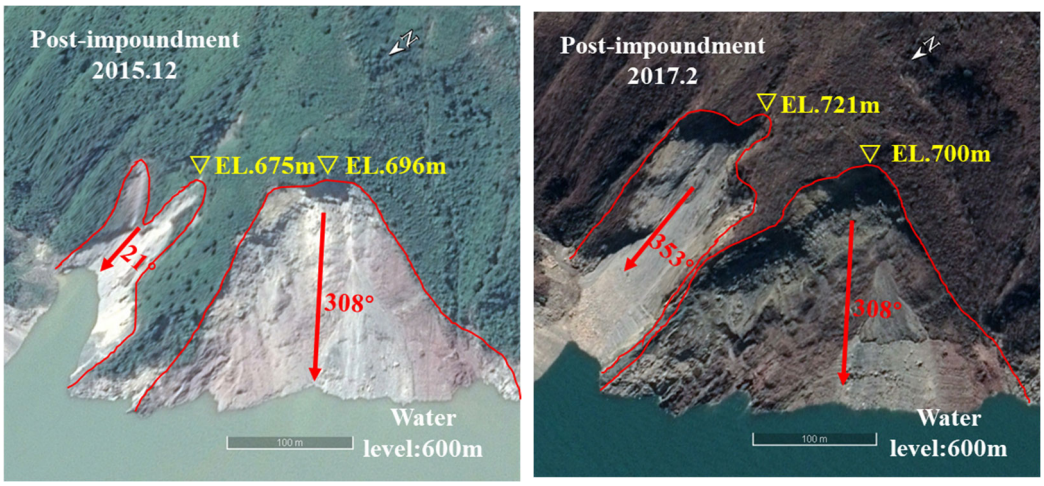

(**c**) (**d**)

Figure 4. Multi-temporal images of the Shangtianba landslide. (**a**) May 2013 before impoundment; (**b**) April 2014 after impoundment; (**c**) December 2015 after impoundment; (**d**) February 2017 after impoundment. The white font indicates the image date and the reservoir water level. The yellow font indicates the elevation of the highest point of the landslide rear edge. The red font indicates the landslide sliding direction. "EL" represents elevation.

(4) Interpretation result verification. To improve the precision of the inventory from remote sensing interpretation, a detailed geological field investigation lasting for one week in September 2021 was carried out in the Xiluodu reservoir area. For newly developed landslides with clear boundaries and significant color differences from the surrounding environment, we conducted a quick verification along both sides of the entire reservoir. Then, for five old landslides with unclear boundaries and deformation conditions, we carried out detailed investigations, corrected their boundaries, and identified the current deformation signs. Photos from the field survey are shown in Figure S2.

3.2. Estimating the Landslide Erosion Rates for the Xiluodu Reservoir

Landslide erosion rates, which consider both landslide volume and time factors, can help to assess the response of bank slope destabilization to anthropogenic forcing. We estimated the landslide erosion rate in the study area using landslide volume. It is difficult to determine the landslide volume, which requires information about the surface and subsurface geometry of the landslide. This information is hard and costly to obtain, especially when a large number of landslides in an area needed to be investigated [45,46]. Currently, most studies achieve this by using empirical relationships linking landslide volume to geometrical measurements, primarily the landslide area [47–50]. In this study, the landslide volume is estimated using a volume–area scaling relationship proposed by Simonett [47], as shown in Equation (1).

$$V = \alpha A^{\gamma} \quad (1)$$

where V and A denote the landslide volume and area, respectively, and α and γ are power-law scaling parameters. Guzzetti et al. [49] analyzed the volume–area relationship of 677 landslides worldwide. These landslides originated from diverse terrains and climatic conditions and were triggered by various factors. The study found a consistent relationship between landslide volume and area, all conforming to the volume–area empirical equation. Numerous studies have produced similar results [47,48,51–55], indicating that the volume–area empirical equation can be applied to landslides of various scales and geological conditions.

Since our study focuses on landslides from 2010 to the present, it has been very difficult to obtain the actual measured volumes of past landslides. So, Equation (1) cannot be applied for regression analysis. The landslide dataset compiled by Larsen et al. [50] is currently the most comprehensive statistical database available, with high credibility and accuracy. Considering that the Xiluodu reservoir area mainly features shallow, small-scale landslides, predominantly rockslides, we selected the parameters $\alpha = 0.146$ and $\gamma = 1.332$ from Larsen's formula [50], derived from a global dataset of 4231 landslides. However, this method of parameter selection has limitations, as it does not consider changes in the hydrological conditions of the Xiluodu reservoir area. But we found that the evolutionary trend was not affected by the size of the parameters. Therefore, the evolution trend of landslide erosion rates obtained in this study is still credible.

During the landslide interpretation process, certain images were obscured by clouds and mist, hindering accurate identification of landslides. This led to some uncertainty regarding the precise timing of landslide development. To mitigate errors associated with temporal uncertainty, we took the three years before impoundment as the first interval, and every two years as intervals after impoundment. Then, we calculated the probability density $p(A)$ of landslide area A with Equation (2) [56].

$$p(A) = \frac{1}{N_T}\frac{\delta N}{\delta A} \tag{2}$$

where N_T is the total number of landslides, δA represents any increment in area, and δN is the number of landslides with areas between A and $A + \delta A$. We divided the landslide area into 7 intervals: 0–500, 500–1000, 1000–5000, 5000–10,000, 10,000–50,000, 50,000–100,000, and 100,000–500,000. The corresponding probability densities $p(A)$ for each interval were calculated, and the results are shown in Table S2. The landslide volume of the ninth to tenth year after impoundment was directly calculated using Equation (1) since only two landslides occurred.

The landslide probability density–area distributions of five periods fit a three-parameter inverse-gamma distribution [56] with Equation (3).

$$p(A) = \frac{1}{a\Gamma(\rho)}\left[\frac{a}{A-s}\right]^{\rho+1}\exp\left[-\frac{a}{A-s}\right] \tag{3}$$

where a, ρ and s are empirical parameters (Table S3), and $\Gamma(\rho)$ is the gamma function of ρ. The landslide probability density–area distributions are shown in Figure S3, and the R^2 of the curve fits are all above 0.9.

Following Malamud et al. [56], we numerically solved for the mean landslide volume of each period using Equation (4).

$$\overline{V} = \alpha\int_{A_{\min}}^{A_{\max}} A^{\gamma} p(A)dA \tag{4}$$

The total landslide volume was determined by multiplying the mean landslide volume by the total number of landslides in each period. Finally, the erosion rate $\dot{h}$ is given by Equation (5).

$$\dot{h} = \frac{\overline{V}N_T}{A_d T} \tag{5}$$

where A_d is the drainage area of the Xiluodu reservoir, and T is the time period. In this study, the pre-impoundment and post-impoundment landslide erosion rates were averaged over three- and two-year periods, respectively.

4. Results

4.1. The Evolution of Landslide Frequency and Scale

Based on the landslide dataset of the Xiluodu reservoir area, we quantified the landslide frequency over six periods by calculating the ratio of landslide numbers in each period to the total number of 536 (Figure 5). The horizontal axis represents the duration of reservoir impoundment, where "0" signifies the three years before impoundment. The data show that during the initial two years after impoundment, the landslide frequency significantly increased compared to before impoundment and then decreased annually. Most landslides occurred within the first four years after impoundment, while within the ninth to tenth year after impoundment, the landslide frequency was smaller than before impoundment.

Figure 5 also shows the variation in landslide scale over time, quantified by the average landslide area. For the pre-impoundment period and the first two years after impoundment, we used the total landslide area for calculations. For the other four periods, we considered only the expanded areas and newly developed landslides. The results show that during the initial two years after impoundment, the average landslide area increased by approximately two times compared to pre-impoundment. The area continued to expand from the third to fourth years after impoundment. Then, the landslide scale decreased continuously from the fifth to sixth years after impoundment, and decreased to smaller than pre-impoundment in the ninth to tenth years after impoundment.

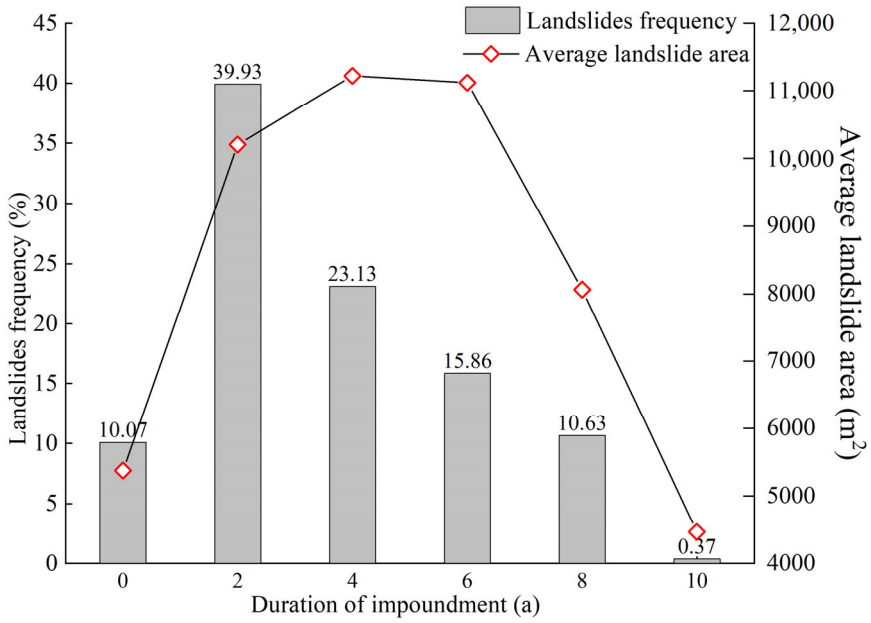

Figure 5. The variation in landslide frequency and scale before and after impoundment. 'a' menas the unit 'year'.

4.2. The Evolution of Landslide Erosion Location

To understand the landslide evolution caused by reservoir impoundment, we analyzed the spatial dispersion or concentration of landslide occurrence. As indicated in Figure 6, the landslides were distributed in a dispersed scope with a distance reaching 2400 m from the river water surface under natural conditions before impoundment. Comparatively, the landslides concentrated 0~200 m above the dead water level after reservoir impoundment, including the reservoir water fluctuation zone. Within the initial two years after impoundment, many landslides occurred under the dead water level, corresponding to the reservoir inundation zone. The standard deviation was used to analyze the

dispersion degree of landslide distribution (the dashed line in Figure 6). The results show that the landslide distribution was more concentrated near the water level after impoundment. After experiencing a relatively dispersive occurrence in the first two years due to the drastic change in hydrological conditions, the landslide distribution became more concentrated in the third to fourth years. After that, it began to disperse gradually in the following years, suggesting that the influence of reservoir water fluctuations on landslide occurrence may tend to diminish, approaching the pre-impoundment condition in the future.

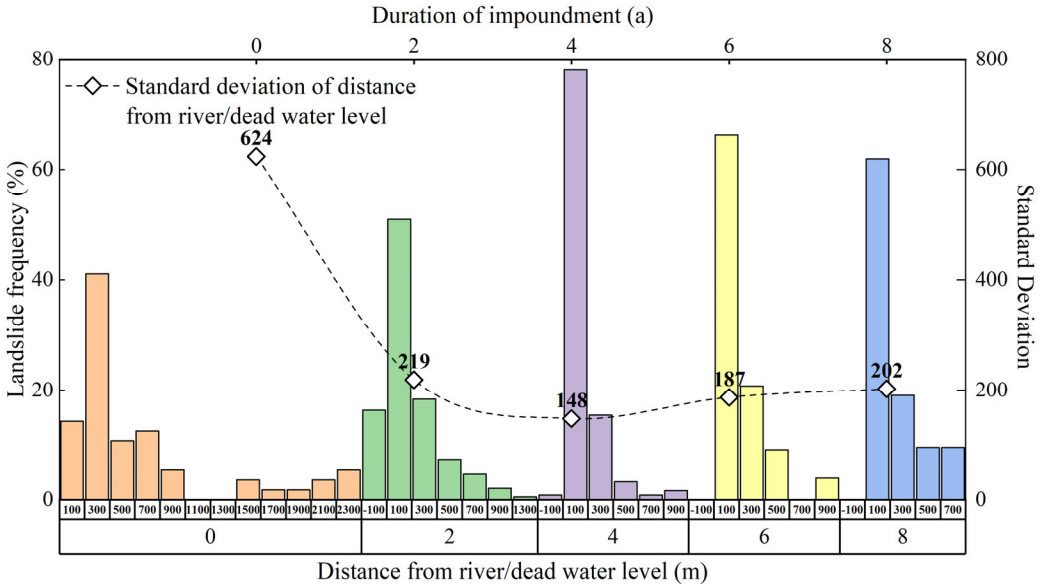

Figure 6. The distance from the river/dead water level of landslides before and after impoundment. The lower x axis represents the midpoint of the distance interval. 'a' means the unit 'year'.

4.3. The Evolution of Erosion-Prone Topography

To describe the landslide incidence in topographic factors (Figure 7), we used the index of landslide concentration (LC), which is the number of landslide sources per square kilometer of surface area [57]. Figure 7a shows the relation of landslides and the LC before and after impoundment with the elevation. Most of the reservoir-induced landslides occurred in the range of 500–900 m, which accounted for 87.3% of the total. According to the statistical results, landslides before and after impoundment both increase with an increase in slope elevation until the maximum is reached at 600–700 m and then decrease. LC has a similar trend and reaches its largest in the elevation category of 600–700 m. The difference is that landslide sources only appear above 600 m before impoundment, whereas 11.8% of reservoir-induced landslide sources are distributed within the 400–600 m range. As shown in Figure 3, the 400–600 m range corresponds to the elevation from the Jinsha River's water surface before impoundment to the normal impoundment level after impoundment. Therefore, reservoir impoundment disturbance may be the reason for landslide development in the 400–600 m range.

The relationship between landslides and the corresponding slope gradient categories was examined, as shown in Figure 7b. Both before and after impoundment, landslides are predominantly concentrated in the range of 20–50°, accounting for 88% and 80% of the total, respectively. Due to the limited area larger than 60°, only a small number of landslides occurred there. The LC after impoundment follows the fitting function $F = 0.29 - 0.24 * e^{-2.60 \times 10^{\wedge} - 6 * x^{\wedge} 3.74}$ with $R^2 = 0.99$ with changes in slope gradient, gradually increasing with the slope and slightly decreasing when the slope exceeds 50°.

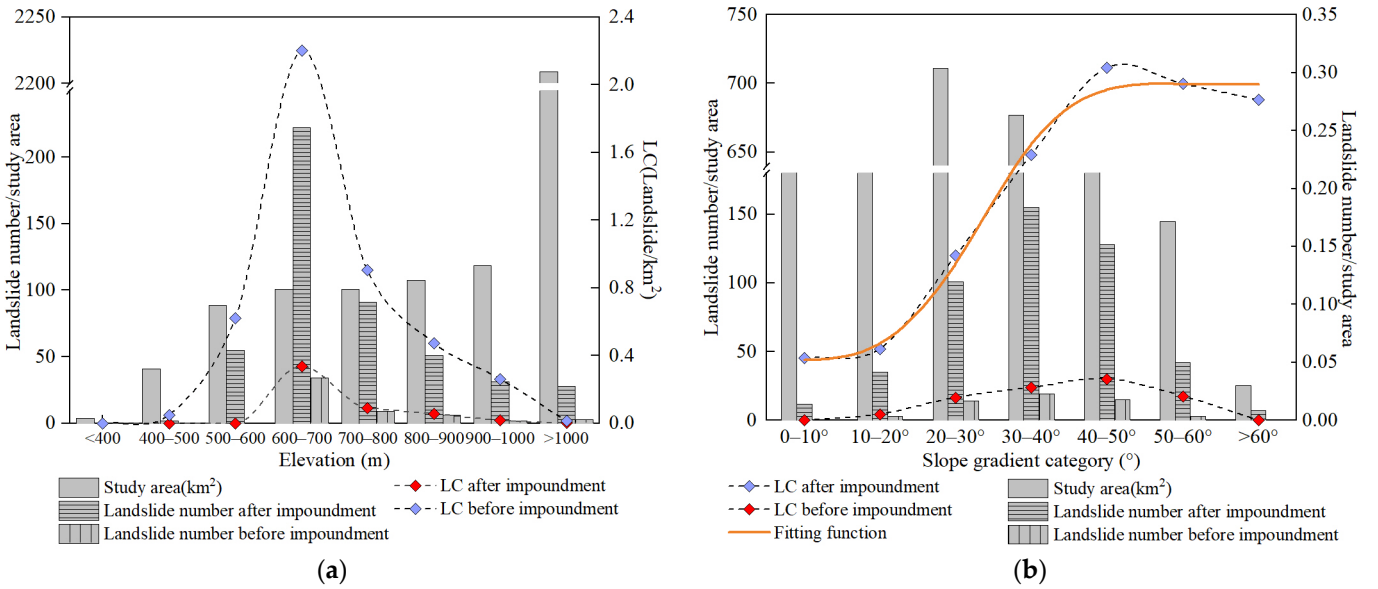

Figure 7. Landslide distribution with topographic factors. (**a**) Relation between landslides and elevation; (**b**) relation between landslides and slope gradient.

4.4. The Evolution of the Erosion-Prone Stratum

Lithology is an important factor controlling the distribution of landslides. Figure 8 shows the relationship between landslides and the strata. The results indicate that the Sinian system Dengying formation (Zz_2dn^1, Zbd) has the highest LC before and after impoundment, with the main lithology being fragmented dolomite (Table S1). The landslide occurrence after impoundment of the lower Permian (P_1), Silurian (S), Ordovician (O), Cambrian (∈), and the Sinian system Chengjiang formation (Zz_1c) all increase compared to before impoundment. These strata have weak lithology or weak interlayers, dominated by shale, mudstone, siltstone, etc. (Table S1), whose strength is susceptible to degradation when exposed to water.

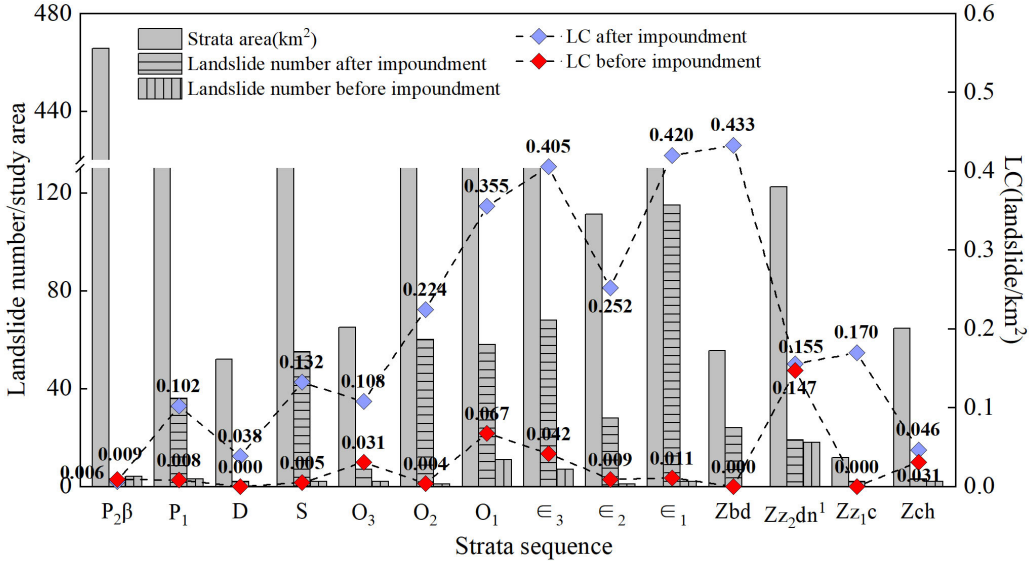

Figure 8. Landslide density in different strata (rock type; see Table S1) before and after impoundment.

4.5. The Evolution of Landslide Erosion Rate

Compared to analyzing landslide numbers, landslide erosion rates consider both landslide volume and time factors, providing a more accurate assessment of bank slope

destabilization in response to reservoir impounding disturbance. Figure 9 shows the landslide erosion rates before and after impoundment. The results illustrate that the landslide erosion rate was 0.44 mm/a before impoundment and 5.16 mm/a in the initial two years after impoundment, representing a twelvefold increase. Within the third to tenth years after impoundment, the landslide erosion rate decreased over time. And especially during the ninth to tenth years after impoundment, the landslide erosion rate was lower than it was before impoundment. This means that the bank slopes reached a more stable state after impoundment than before impoundment. To further demonstrate this result, we fitted the landslide erosion rate after impoundment with the duration of reservoir impoundment. The fitting formula is $y = 10.17e^{-0.34x}$, with $R^2 = 0.98$, and the 95% confidence intervals for the parameters are [7.51, 12.83] and [−0.43, −0.26], respectively. The negative exponential distribution suggests that the landslide erosion rate will continue to decrease, which implies that the bank slopes in the Xiluodu reservoir area will be more stable than before impoundment in the future.

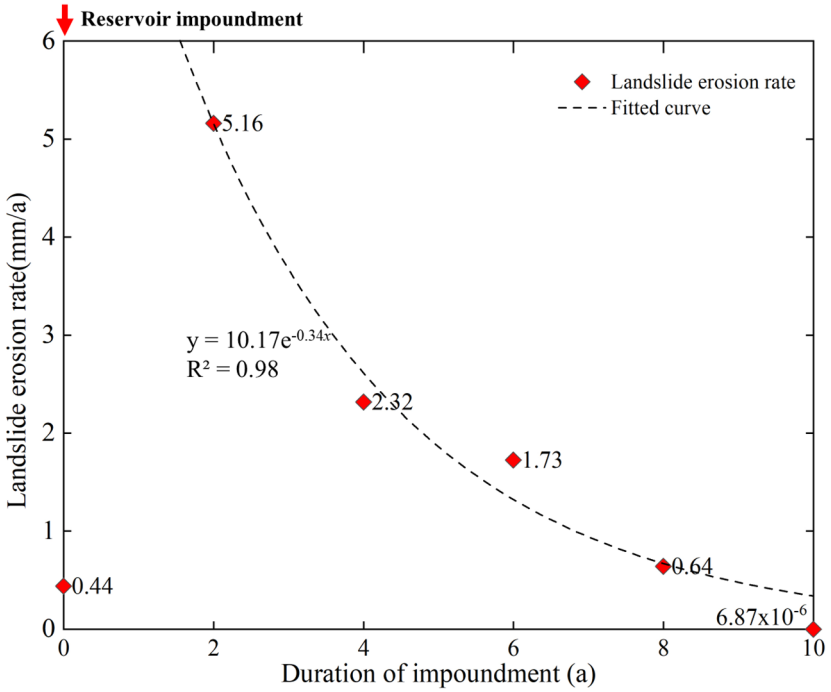

Figure 9. The variation in landslide erosion rate over time. The red arrow indicates the time when the reservoir began impoundment.

5. Discussion

5.1. The Long-Term Evolution Trend of Reservoir-Induced Landslide Erosion

To further explore the evolution trend, we interpreted the reservoir-induced landslides in the Liyuan Reservoir of the Jinsha River using multi-temporal images. The Liyuan Reservoir is in the midstream of the Jinsha River (Figure 10) and began impoundment in 2014. It has now been impounded for ten years. The landslides interpreted in this reservoir are concentrated between 2014 and 2016, with a total of 63 landslides. After 2016, no further reservoir-induced landslides developed. This indicates that the initial two years of impoundment represent the peak period for reservoir-induced landslides in the Liyuan Reservoir. Currently, the slopes appear to have stabilized, consistent with the pattern observed in the Xiluodu reservoir area.

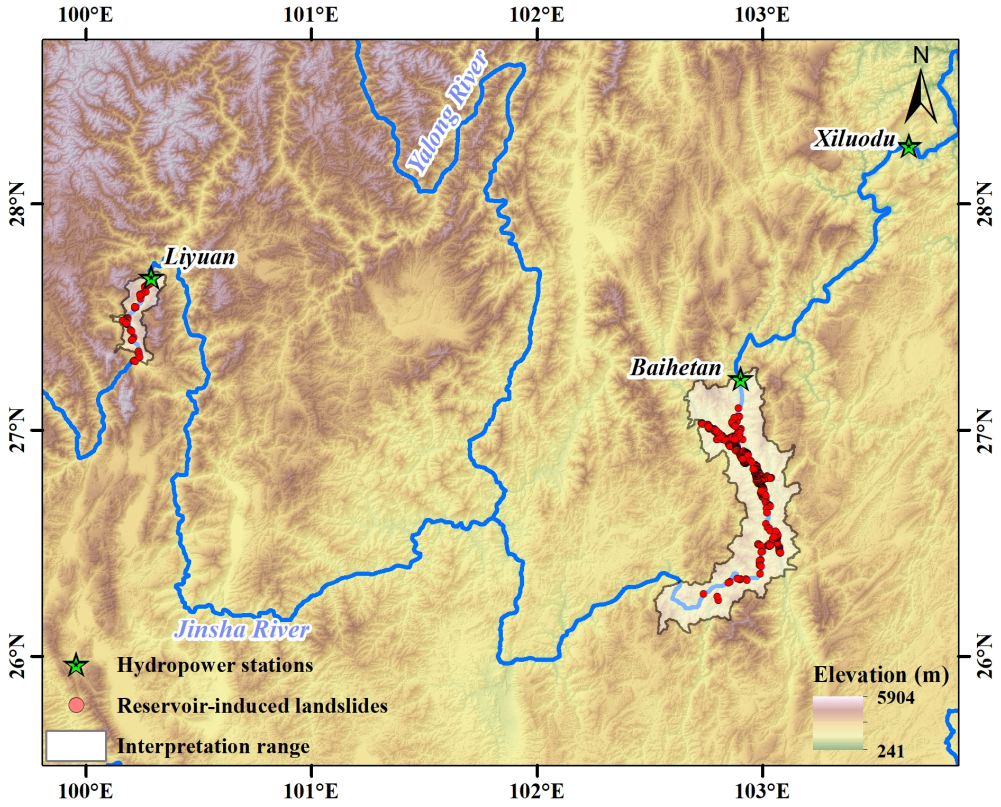

Figure 10. The distribution of reservoir-induced landslides in the Baihetan and Liyuan reservoirs.

In addition to the reservoirs in the Jinsha River, we examined existing reports about the temporal evolution of reservoir-induced landslides in other reservoirs, including Roosevelt Lake [2], the Huanglongtan Reservoir [18], the Three Gorges Reservoir [21], and 60 published cases [19]. When comparing these global cases, we considered the differences in geological, hydrological, and operational conditions that may influence landslide behavior. Geologically, the landslide-prone strata in the Three Gorges and Xiluodu reservoir areas predominantly consist of weak or weakly bedded rock formations. In contrast, landslides in the Huanglongtan Reservoir are mainly found in strata with well-developed rock schistosity and Quaternary loose deposits. Roosevelt Lake's landslides mainly occur in relatively unconsolidated Pleistocene glaciofluvial deposits. Across all these reservoir areas, the landslide-prone strata share a common characteristic: they are water-sensitive weak layers. Hydrologically and operationally, the Three Gorges Reservoir took six years to reach its normal water level, experiencing three significant phases of water level rise: 75 m, 21 m, and 30 m. After reaching its normal operation, the water level fluctuated by about 30 m. The Huanglongtan Reservoir took approximately three years to reach its normal water level, with water level fluctuations between 20 m and 27 m. The Xiluodu reservoir reached its normal impoundment level in about two years, with two significant water level rises of 140 m and 60 m, and fluctuations of up to 60 m. Due to differences in reservoir scale and water level fluctuations, the number of landslides triggered during impoundment to the normal water level varies significantly: 402 in the Three Gorges Reservoir, 225 in the Xiluodu reservoir, and only 28 in the Huanglongtan Reservoir. We plotted the variation in landslide frequency relative to the duration of reservoir impoundment for these reservoirs in Figure 11a. The plot shows that the reservoir-induced landslides mainly occurred during the impoundment stage despite differences in scale, water fluctuations, and geological conditions. Although numerous landslides are triggered again by heavy rain or a sharp drop in the reservoir water level, the overall trend indicates a gradual decrease in landslide frequency.

When all reservoir-induced landslide data were plotted on the same *x*-axis (Figure 11b), we observed that all the reservoirs tended to stabilize after about five years of reservoir impoundment. In the Three Gorges Reservoir, a significant fluctuation in the number of landslides occurred in the sixth year due to the multi-stage impoundment approach, but the bank slope quickly stabilized afterward. In the Huanglongtan Reservoir area, the number of landslides that developed in the tenth year after impoundment exceeded the number during the initial impoundment stages, primarily influenced by prolonged and heavy rainfall events.

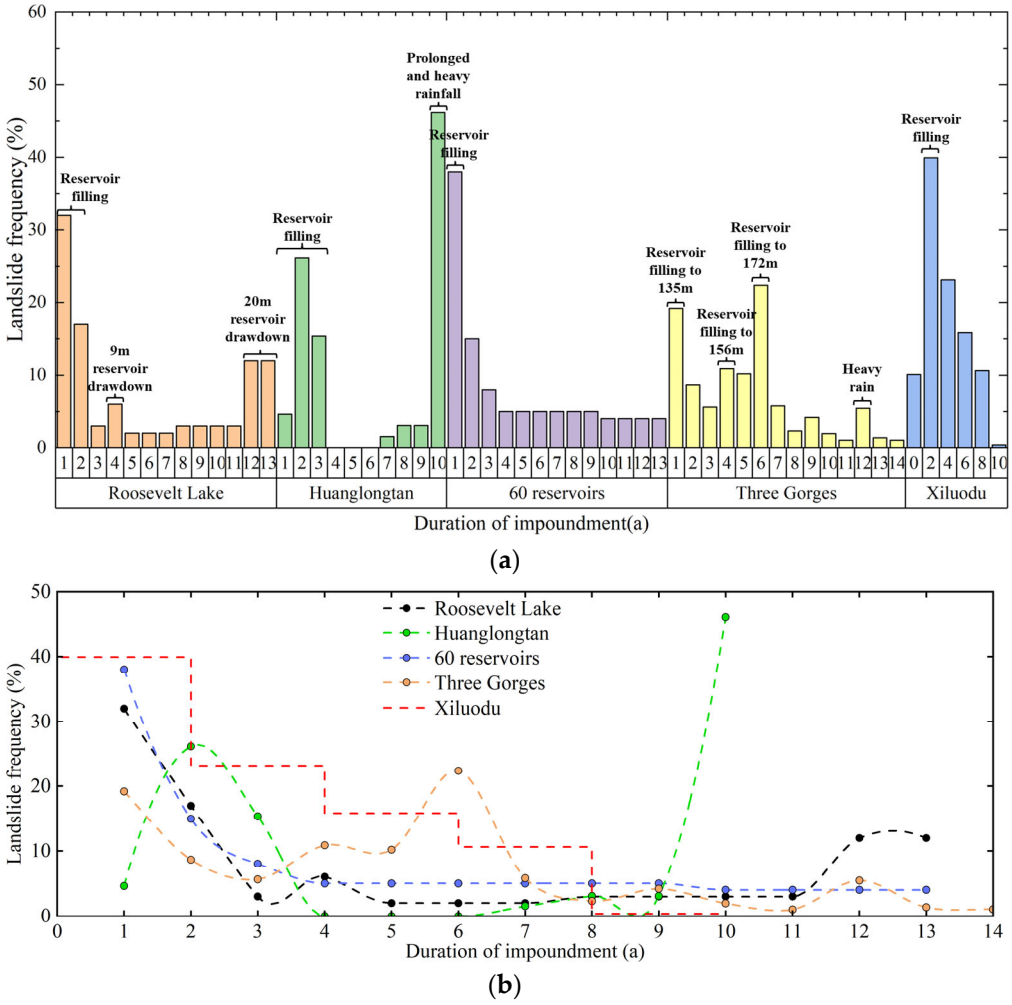

Figure 11. The relationship between the frequency of reservoir-induced landslides and the duration of impoundment. (**a**) The data are plotted separately for Roosevelt lake [2], Huanglongtan [18], 60 Reservoirs [19], Three Gorges and Xiluodu Reservoir. The text in the figure explains the reasons for the relatively high occurrence of landslides during the corresponding period. (**b**) All reservoirs use the same *x*-axis.

Compared to existing research, our study not only analyzed the variation in landslide frequency (Figure 5) with the duration of reservoir impoundment, but also examined the changes in landslide magnitude (Figure 5) and spatial distribution (Figure 6) over time. These results demonstrate the gradual stabilization of bank slopes and provide more evidence to corroborate temporal evolution trends. However, our method was limited to identifying landslides with obvious deformation signs and failed to capture the evolutionary trends of slopes with long-term slow deformation. According to existing studies, the long-term evolutionary trends of slowly deforming slopes align with our observed patterns. Li et al. [44] used InSAR to monitor unstable slopes before and after the

impoundment of the Xiluodu reservoir. The results showed that 143 unstable slopes (94% of the total slopes) occurred during the first three years after reservoir impoundment. From October 2016 to October 2018, only 9 unstable slopes occurred, and no new unstable slopes have occurred since October 2018.

This study interpreted landslides newly developed three years prior to impoundment and calculated the pre-impoundment landslide erosion rates, establishing a baseline for assessing post-impoundment erosion levels. By comparing the landslide erosion rate before and after reservoir impoundment (Figure 9), we can predict the long-term evolution of bank slope stability. The results indicate that the Xiluodu bank slope will be more stable in the future than it was before reservoir impoundment. In other words, reservoir construction is beneficial to bank slope stability in the long run.

5.2. The Identification of Reservoir-Induced Landslide Erosion Process

Based on the spatiotemporal distribution and evolution of reservoir-induced landslide erosion rates, along with field monitoring data from individual case studies, we divided the deformation of the reservoir bank slope into three stages.

5.2.1. The Period of Concentrated Landslide Outbreaks: The First Stage Is the Period of Reservoir Impoundment to the Normal Impoundment Level (Within About Two Years)

During this stage, the landslide erosion rate increased dramatically (Figure 9), likely due to reservoir inundation. For instance, the Shangtianba landslide in the Xiluodu reservoir area showed no signs of deformation before impoundment (Figure 4a), but small-scale bank collapses occurred after the water level rose to 560 m (Figures 4b and 12a). The initial rise in reservoir level triggered the reactivation of the Niulanjiang [58] and Yulinerzu landslides [59] (Figure 12a). During the initial impoundment stage, the Maoping landslide developed many cracks and settlement at the front (Figure 12b) [8]. Moreover, the deformation of the Guobu slope also showed a positive correlation with reservoir water levels (Figure 12c) [13].

The impact of reservoir inundation on bank slope stability can be primarily attributed to two factors. The first is the effect of reservoir inundation on the mechanical properties of materials. The increase in water content will decrease the cohesion and internal friction angle of the rock and soil mass [8,60–62], thereby reducing the shear strength of the slope. As a result, strata with fractured rocks, weak lithology, or weak interlayers are more prone to landslides after reservoir impoundment (Figure 8). The second is the hydraulic effects of reservoir inundation, including the floating effect and the seepage pressure effect. The floating effect occurs as the reservoir water level rises, the submerged volume of the slope increases, and the water exerts an upward buoyant force on the landslide body. This reduces effective stress, thereby decreasing the shear strength of the slope, as shown by the Mohr circle in Figure 13a. The seepage pressure effect means that during a rapid rise in water level, a hydraulic head difference is formed between the inside and outside of the slope (Figure 13a), thereby generating inward seepage pressure on the slope. This can improve the bank slope stability, mainly for weak permeability slopes. It should be noted that the permeability and hydrogeological structure of the slope can influence hydraulic effects [63]. For example, the slide mass of the Yulinerzu landslide [59] in the Xiluodu reservoir area has a high permeability coefficient. When the reservoir water level changes, the groundwater level within the landslide body synchronizes with the reservoir level. At this time, the adverse impact of the floating effect is more significant than the beneficial impact of the seepage pressure effect. The Xingguangsanzu (XGSZ) toppling instability is caused by an underdip bedding rock slope [64], and the Yanwan (YW) toppling instability is caused by an anti-dip bedding rock slope in the Xiluodu reservoir area [65]. Their geological conditions are essentially the same, but differences in slope structure led to

variations in permeability, resulting in different degrees and modes of deformation. XGSZ shows a large permeability difference between the front and rear edges. It causes the seepage and floating effects induced by reservoir water level changes to concentrate mainly in the lower part of the slope, leading to a higher deformation rate in that area. In contrast, YW has a minimal permeability difference between the front and back edges, and the fault zone in the middle of the slope has strong hydraulic conductivity. This feature allows the hydraulic effects to significantly influence the entire slope. This causes the deformation mode of XGSZ to be retrogressive, while that of YW is progressive.

During the initial impoundment stage, reservoir inundation primarily triggered new small-scale landslides and reactivated old ones, and may have contributed to the formation of tension cracks at the top of the slopes (Figure 13a). Precipitation is primarily discharged through surface runoff due to the limited number and size of cracks on the slope, and thus, is not the main trigger of bank slope failure.

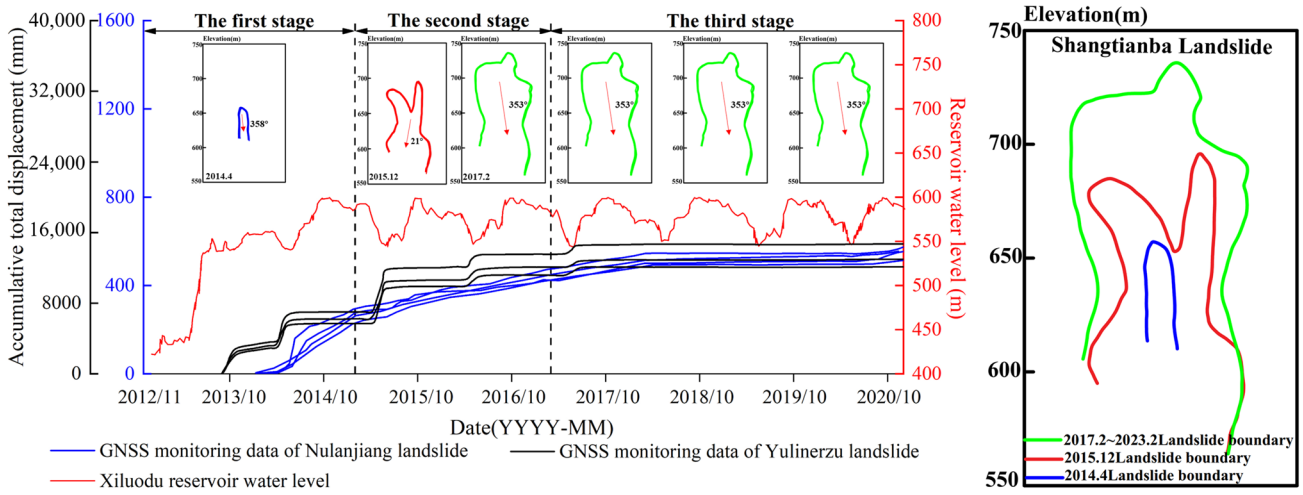

(**a**)

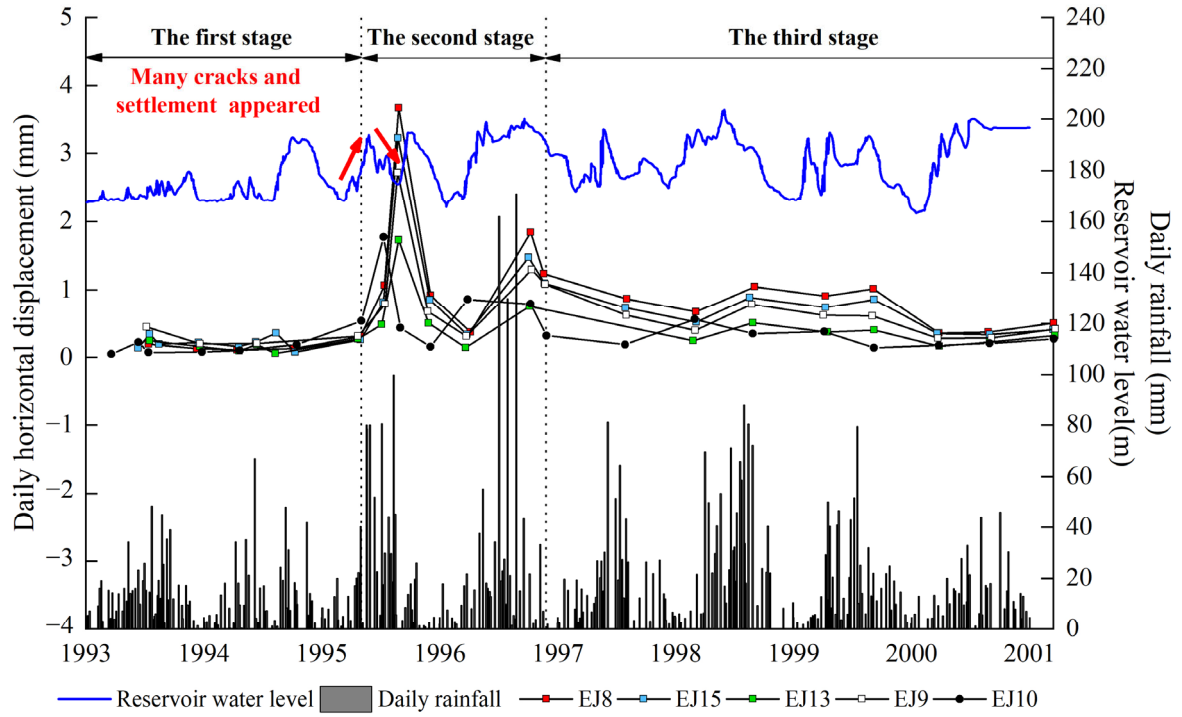

(**b**)

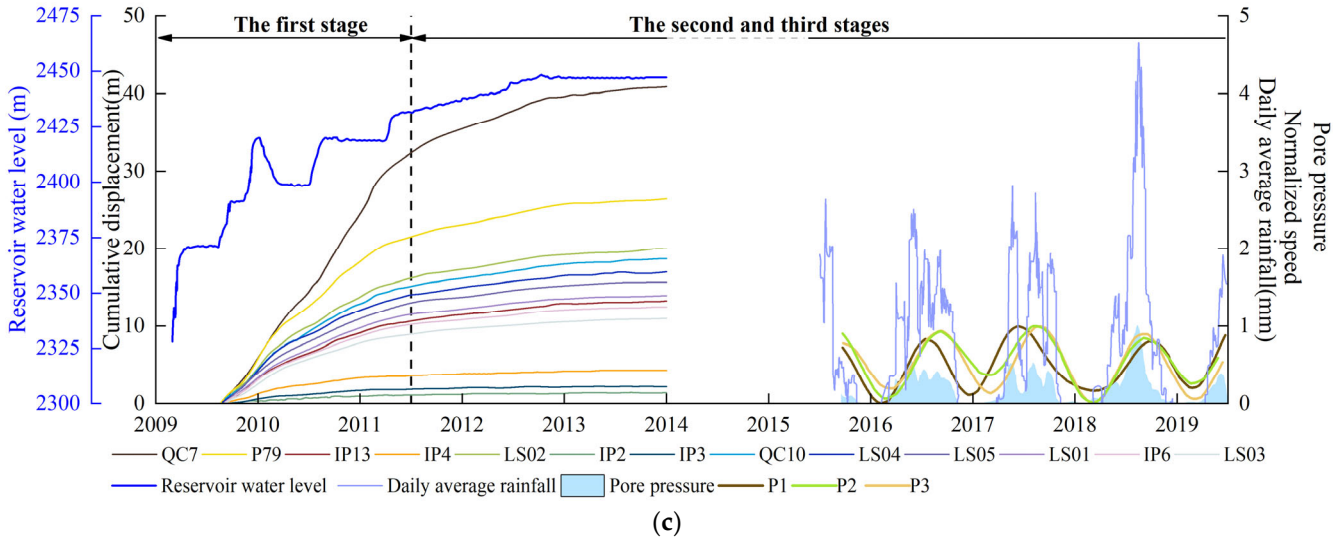

(**c**)

Figure 12. Comparison between landslide deformation, rainfall, and reservoir level. (**a**) Shangtianba, Niulanjiang [58], and Yulinerzu landslides [59] of Xiluodu reservoir area, and the arrows indicate the direction of the landslide movement.; (**b**) Maoping landslide of Geheyan reservoir of Qingjiang River, Hubei Province, China (adapted from Qi et al. [8]), and the red arrows indicate the rise and fall of the water level; (**c**) Guobu slope of Laxiwa reservoir in Qinghai, China (adapted from Shi et al. [13]).

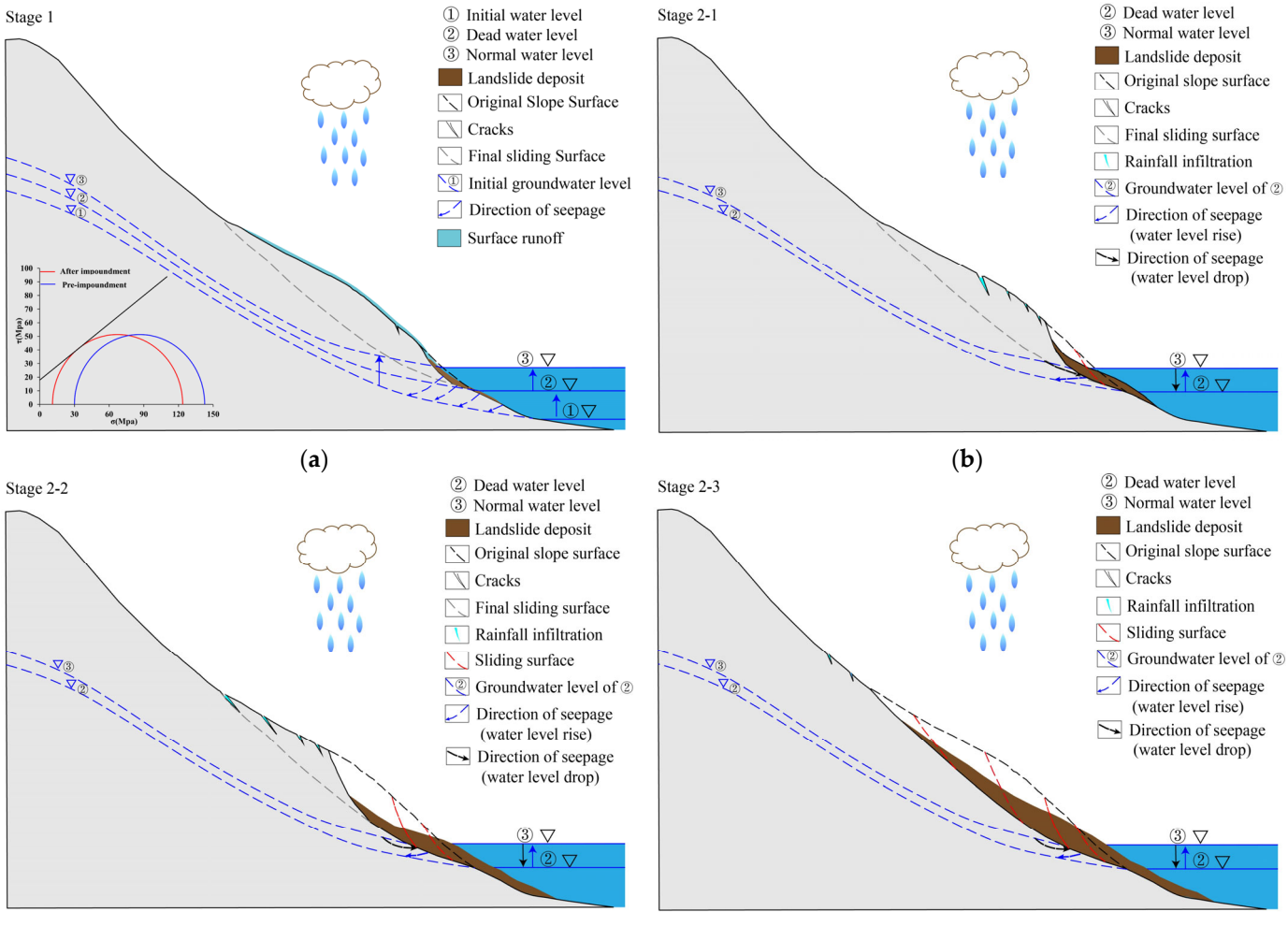

(**a**) (**b**)

(**c**) (**d**)

Figure 13. A reservoir-induced landslide expansion pattern diagram. (**a**) The collapse of the foot of the slope in the initial impounding stage, and a schematic diagram and Mohr circle of the change in

stress after impoundment; (**b**) rainfall infiltration into the cracks; (**c**) the retreat of the landslide boundary under the combined effect of reservoir water fluctuations and rainfall; (**d**) landslide accumulation on the foot of the bank slope.

5.2.2. Landslide Development Slowing Phase: The Second Stage Is the First Few Years of Stable Reservoir Operation, Approximately the Third to Fourth Years After Impoundment

In this stage, the reservoir entered the stable operation phase. The two major deformations of the Maoping landslide in the second stage occurred after the water level drawdown and following heavy rainfall, respectively (Figure 12b). This suggests that the combined effect of water level fluctuations and precipitation became the dominant controlling factor in this stage. Previous studies have shown that the impact of sudden water level drawdowns [8,66,67] and extreme rainfall is particularly significant. When the water level rapidly and significantly decreases, the delayed change in pore pressure within the slope can lead to a short-term increase in the hydraulic gradient [68–70], resulting in seepage outwards from the slope (Figure 13b), consequently increasing the sliding force. Additionally, it has been found that the mechanical properties of landslides change significantly with an increasing number of reservoir water level cycles. Model test results from Wu et al. [71] show that as the number of reservoir water level cycles increases, the pore water pressure and soil pressure in the reservoir landslide exhibit an oscillating increase. The accumulation of pore water pressure during each cycle continuously enhances the buoyancy effect on the slope, thereby reducing the effective stress. As a result, the sliding force increases, and the resisting force decreases, causing a reduction in landslide stability with the increasing number of water level cycles. Meanwhile, water level fluctuations create a dry–wet cycling zone at the slope's front edge, significantly weakening the rock and soil mass strength of the slope [72]. A numerical simulation by Zhang et al. [73] showed that with thane increasing number of dry–wet cycles, the landslide safety factor gradually decreases, especially showing a significant reduction during the first five cycles. According to these studies, water level fluctuations mainly affect the submerged area at the slope's front edge [9,72,74,75]. Following the initial toe collapse of the first stage (Figure 13a), water level fluctuations cause more unstable rock and soil deposits in the valley, gradually impacting the upper slope and showing a typical retrogressive failure process (Figure 13b–d). Large-scale model tests simulating a loose sandy silt slope also show that, under the influence of water level fluctuations, the landslide deformation mode is characterized by multiple retrogressive rotational slides [68].

Apart from water level fluctuations, precipitation is also an important triggering factor for landslide deformation at this stage, with its impact primarily reflected in two aspects. Firstly, rainfall infiltration affects the mechanical properties of the soil and rock mass, increasing the water content in the slope and thereby reducing its shear strength. Secondly, precipitation infiltrates the slide mass through surface cracks, generating high pore pressure, which increases the sliding force and decreases the mechanical strength of the rock and soil mass of the slope [8]. Existing studies indicate that the intensity and duration of rainfall, along with the slope's permeability, together determine its impact on landslide deformation. High-intensity short-duration rainfall is more likely to trigger sudden landslide movement [76,77]. It rapidly infiltrates the surface layer of the slope and leads to a significant increase in pore water pressure in a short time [72]. This is more likely to cause shallow sliding, especially in low-permeability slopes [78]. Alternatively, long-duration low-intensity rainfall gradually infiltrates deeper into the landslide, accumulating deep-seated pore water pressure over time. This cumulative effect may trigger delayed deep-seated landslide instability after the rainfall ends, with the lag effect being particularly pronounced in low-permeability slopes [77].

The combined effects of water level fluctuations and rainfall accelerate and intensify slope instability. For example, the initial reservoir impoundment and water level fluctuations promoted the development of slope cracks, increasing slope permeability and making rainfall infiltration easier (Figure 13b). The combined effects of water level drawdown and rainfall enhance the lag effect of pore water pressure changes within the slope, leading to more intense fluctuations in pore water pressure both inside and outside the slope, thereby increasing slope instability. Additionally, the coupling of these two factors makes the deformation pattern of the bank slope more complex. Numerical simulation results show that rainfall induced progressive instability in the upper slope, while water level fluctuations triggered retrogressive collapse at the slope toe, resulting in a forward-pulling effect [9,72,74,75].

Due to the landslides and cracks that occurred during the first stage, the slope stability was reduced, leading to relatively severe landslide erosion under the combined influence of reservoir water fluctuations and rainfall during the first few years of stable reservoir operation. However, with the cyclical water level fluctuations and repeated rainfall, the slope has gradually adapted to these environmental changes, resulting in increased stability. For instance, as the number of water level cycles increases, the deformation of the Yulinerzu landslide during water level drawdown becomes progressively smaller (Figure 12a). Consequently, the severity of landslide erosion has shown a decreasing trend compared to the first stage (Figure 9).

5.2.3. The Period of Landslide Development Tending to Stabilize: The Third Stage Is After About Five Years of Reservoir Impoundment, During Which Rainfall Gradually Becomes the Primary Controlling Factor

In the third stage, the variation in regional landslide erosion (Figure 9) and individual landslide deformation (Figure 12) over time shows that the bank slope stability at this stage reached a more stable state compared to the previous two stages. The slope gradually adapted to the hydrologic environment characterized by cyclical fluctuations in water level. However, landslide deformation fluctuated slightly during the rainy seasons, such as the deformation in 1999 at the Maoping landslide (Figure 12b) and from 2016 to 2019 at the Guobo slope (Figure 12c). This indicates that rainfall, especially extreme rainfall, has become the primary controlling factor.

Under the combined influence of rainfall and water level fluctuations in the first two stages, the movement of some reactivated landslide masses undergoes a self-stabilizing process as displacement accumulates. Existing studies [15,59] conceptualize the reactivated landslide mass as two blocks: an upper block with a steeper sliding surface and a lower block with a gentler sliding surface. The rainfall induces back-pushing of the upper block and the reservoir induces fore-pulling of the lower block [9,74]. Therefore, the unstable upper block of the landslide gradually shifts downward, reducing its weight. Meanwhile, the mass of the lower block increases, anchoring it more securely to the gentler sliding surface. This mass transfer results in a redistribution of gravitational forces, improving overall stability. Obviously, this deformation mode is more suitable for landslides with chair-shaped sliding surfaces or arc sliding surfaces. Evidence from other studies indicates that the toppling deformations in the study area also tend to stabilize during this stage [64]. Significant increases in the deformation of the XGSZ and YW toppling instabilities occurred within the first five years after reservoir impoundment. Five years later, the deformations of XGSZ and YW formed a relatively balanced confrontation environment with water-level fluctuations. However, the stability mechanisms for toppling deformations and other types of landslides still require further research. It is speculated that the combined disturbances from reservoir impoundment, water level fluctuations, and rainfall caused instability in the bank slope, reducing its potential energy. Meanwhile,

landslide debris accumulating at the foot of the slope (Figure 13d) increases pressure on the slope surface at the slope foot, enhancing its resistance to sliding. Therefore, the landslide erosion rate decreased at this stage (Figure 9).

Figure 9 shows that the landslide erosion rate in the ninth to tenth years is lower than before impoundment, indicating that the bank slopes have become more stable than they were before impoundment. This trend is due to changes in the factors triggering landslides before and after impoundment. Before reservoir impoundment, river incision and rainfall are the main controlling factors for landslide erosion. After impoundment, the bank slope stability is no longer affected by river incision. In the first period of reservoir impoundment to the normal impoundment level (generally within about two years), reservoir inundation is the main cause of landslide erosion. In the second stage, during the first few years of stable reservoir operation, reservoir water level fluctuations and rainfall become the main factors in landslide erosion. In the third phase, rainfall gradually becomes the primary controlling factor in landslide erosion. Due to the continuous deposition at the foot of the slope from landslide erosion, along with the accumulation of sediment resulting from the weakening of hydrodynamic forces in the reservoir, the bank slopes become more and more stable, and the landslide erosion rate is even lower than that before impoundment.

It should be noted that extreme rainfall or rapid water level decline can still trigger sudden instability in bank slopes. In particular, the frequency of extreme rainfall events has increased globally in recent years (especially for sub-daily extreme rainfall) [79]. For the Jinsha River Basin, the extreme precipitation indices showed a continuous increasing trend from 1961 to 2020 [80]. The variation rates of Rx1day (annual maximum 1-day precipitation), Rx5day (annual maximum 5-day precipitation), and R99p (annual total precipitation when daily precipitation is >99th percentile) were 1.12 mm, 1.21 mm, and 5.87 mm per decade, respectively. From the late 2000s to the late 2010s, these indices exhibited significant fluctuation and an increasing trend. After the abrupt change, the values of Rx1day, Rx5day, and R99p were 58.61 mm/a, 112.73 mm/a, and 93.91 mm/a, respectively, which were 7.4%, 5.7%, and 33.4% higher than before the abrupt change. This indicates that in the past 10 years, extreme precipitation events have been more frequent and intense than during the 1961 to 2000 period. Kaczmarek et al. [16] studied the displacement changes in the Central Landslide in the Włocławek Reservoir over 40 years after impoundment. They found that even after 40 years of impoundment, the landslide still exhibited significant deformation due to extreme rainfall. Based on this, it can be inferred that even if the bank slopes have stabilized after 10 years of impoundment, landslide erosion may still intensify in the future due to increased frequency and intensity of extreme rainfall. Landslides initially controlled by reservoir water levels may become increasingly susceptible to precipitation impacts [14]. Therefore, disaster prevention and mitigation remain essential even for long-term-operating reservoirs.

Building on the above pattern, we predicted the evolution trend of bank slope stability in the Baihetan Reservoir area. Located upstream of the Xiluodu reservoir (Figure 10), the Baihetan Reservoir began impounding in April 2021, reaching a dead water level of 765 m by June. By October 2022, it had reached the normal reservoir level of 825 m. Since then, the reservoir has entered a stable operation phase, with water levels fluctuating between 765 m and 825 m. In this study, a total of 633 landslides were interpreted from April 2021 to March 2024 (Figure 10). Among them, 594 landslides occurred during the first two years after impoundment, accounting for 93.8%. The number of reservoir-induced landslides significantly decreased in the third year after impoundment, with only 39 landslides observed. Based on the three stages we defined, the Baihetan Reservoir area is currently in the second stage, where it is jointly controlled by water level fluctuations and rainfall. Landslide erosion has weakened compared to the first stage, and the bank slopes have

started to stabilize. However, during this stage, the bank slopes are still significantly affected by water level fluctuations and rainfall, and a certain number of disasters may still occur. Therefore, monitoring bank slope stability is essential, especially during extreme rainfall events. The monitoring range can be concentrated on steep slopes, weak geological tectonic zones, lithologically weak areas, and the reservoir water fluctuation zone. It is recommended to manage reservoir water levels through multiple small-scale adjustments, gradually raising and lowering the levels.

This study identifies the long-term trends in bank slope stability in reservoir areas, confirming that reservoir impoundment contributes to the long-term stability of bank slopes. Although our theoretical analysis highlights the impact of pore water pressure changes and reservoir water level fluctuations, relying solely on the regression analysis of existing landslide data is insufficient to uncover the underlying mechanical processes. Therefore, we plan to use physical model experiments or numerical simulations at the reservoir scale to comprehensively investigate the long-term evolutionary mechanisms of bank slope stability. In addition, while visual assessment is a well-established method for multi-temporal landslide mapping, it is inherently subjective and labor-intensive. For multi-temporal landslide detection, previous research [23,81–84] has employed various (semi-)automated tools based on optical satellite time series, such as the combination of machine learning-based classification and object-based image analysis (OBIA) [84]. These methods have shown high accuracy in identifying natural disasters triggered by earthquakes or heavy rainfall. But there has been no automated detection research specifically targeting multi-temporal reservoir-induced landslides. These methods are mostly based on vegetation cover changes for multi-temporal landslide detection. The landslides we identified are relatively small in scale, and their vegetation cover characteristics are hard to distinguish from the soil loss area within the hydro-fluctuation belt of the reservoir. Therefore, existing automated methods may have larger errors in interpreting reservoir-induced landslides. Nevertheless, automated detection methods can eliminate subjectivity in landslide interpretation. In future research, we will further explore the application of these methods and attempt to combine them with visual interpretation to improve the efficiency, accuracy, and robustness of landslide detection. Furthermore, the use of annual observations may result in overlooking shorter-term events or rapid slope deformations triggered by extreme weather. To address this, we plan to enhance the temporal resolution of the data to better capture the dynamic evolution of landslides.

6. Conclusions

In this paper, a total of 54 landslides in the three years before impoundment and 482 reservoir-induced landslides in the ten years after impoundment were identified in the Xiluodu reservoir area through multi-temporal image interpretation. We compared the evolution of landslide frequency, magnitude, spatial distribution, and erosion rate before and after impoundment to clarify the long-term evolution trend of reservoir-induced landslide erosion. Then, by combining the deformation process of typical reservoir-induced landslides, we divided the evolution trend into three stages based on changes in landslide-triggering factors. We attempted to answer whether the impact of reservoirs on the natural environment is positive or negative. The following conclusions were reached.

(1) Most landslides are triggered within about four years after impoundment and are mainly concentrated in the reservoir inundation zone, water fluctuation zone, and strata with fragmented and weak lithology. Reservoir-induced landslides are prone to occurring in areas with elevations between 500 and 900 m and slopes of 20–50°. After five years of impoundment, the change in landslide magnitude and the dispersion of landslide distribution reflect the gradual stabilization of bank slopes and the weakening of reservoir impacts. The landslide erosion rate increases sharply during the initial impoundment period

after impoundment and decreases following a negative exponent relation with increasing impoundment duration, gradually becoming closer to or even lower than before impoundment.

(2) The three stages of the evolution of reservoir bank slope stability are identified. The first stage is the initial impounding period (about two years), which is characterized by small landslides that occur as a result of reducing the shear strength of the bank slope; the second stage is the first few years of stable reservoir operation (approximately the third to fourth year after impoundment), and in this stage, rainfall and reservoir water fluctuations are the main causes of landslide occurrence as they influence the pore water pressure of the bank slope; the third stage is after five years of reservoir impoundment, where the influence of reservoir water fluctuations gradually weakens, and rainfall gradually becomes the primary controlling factor.

(3) Most of the bank slopes worldwide seem to be gradually stabilized in the third stage, with little relation to the scale and geological setting of reservoirs. Even though further evidence is still needed, this study determines that the operation of reservoirs tends to contribute to bank stability and the geoenvironment in the long run, even in a vulnerable active orogenic belt such as the Hengduan Mountain region.

Supplementary Materials: The following supporting information can be downloaded at: www.mdpi.com/article/10.3390/rs17040569/s1, Figure S1: Slope of study area; Figure S2: Field investigation photos of landslides; Figure S3: Landslide probability density–area distribution; Table S1: Stratigraphic units and lithological composition of study area; Table S2: Landslide probability density of different scales; Table S3: Inverse gamma-fitting parameters.

Author Contributions: Conceptualization, S.Q. and S.G.; formal analysis, F.T., S.Q. and S.G.; methodology, F.T., S.Q. and S.G.; investigation, F.T., S.Q., S.G., Y.L. and X.L.; writing—original draft: F.T.; data curation: F.T.; visualization: F.T.; writing—review and editing: F.T., S.Q., S.G., Y.L., X.G., X.L., Y.Z., X.W., X.H., L.M., B.Z. and Z.W.; funding acquisition: S.Q., S.G. and Y.Z.; project administration: S.Q. All authors have read and agreed to the published version of the manuscript.

Funding: This research was funded by the Second Tibetan Plateau Scientific Expedition and Research Program, grant number 2019QZKK0904; the National Natural Science Foundation of China, grant numbers 42422706, 42207205, and 42077266; and the Youth Innovation Promotion Association of the Chinese Academy of Sciences, grant number 2022062.

Data Availability Statement: The data are contained within the article.

Acknowledgments: The author appreciates all the data provided by each open database.

Conflicts of Interest: The authors declare no conflicts of interest.

References

1. Zheng, S.Y.; Li, Z.B. *Landslide Erosion Research*; Yellow River Water Conservancy Press: Zhengzhou, China, 2005. (In Chinese with English Abstract)
2. Jones, F.O.; Embody, D.R.; Peterson, W.L. Landslides along the Columbia River Valley. *Northeast. Washington. U.S. Geol. Surv. Prof. Pap.* **1961**, *367*, 98. https://doi.org/10.3133/pp367.
3. Schuster, R.L. Reservoir-induced landslides. *Bull. Int. Assoc. Eng. Geol*. **1979**, *20*, 8–15. https://doi.org/10.1007/bf02591233.
4. Müller, L. The rock slide in the Vajont Valley. *Rock. Mech. Eng. Geol*. **1964**, *4*, 148–212.
5. Tang, H,; Wasowski, J.; Juang, H.C. Geohazards in the Three Gorges Reservoir Area, China—Lessons learned from decades of research. *Eng. Geol.* **2019**, *261*, 105267. https://doi.org/10.1016/j.enggeo.2019.105267.
6. Dai, F.C.; Deng, J.H.; Tham, L.G.; Law, K.T.; Lee, C.F. A large landslide in Zigui County, Three Gorges area. *Can. Geotech. J.* **2004**, *41*, 1233–1240. https://doi.org/10.1139/t04-049.
7. Skempton, A.W. Bedding-plane slip, residual strength and the Vaiont landslide. *Géotechnique* **1966**, *16*, 82–84. https://doi.org/10.1680/geot.1966.16.1.82.

8. Qi, S.W.; Yan, F.Z.; Wang, S.J.; Xu, R.C. Characteristics, mechanism and development tendency of deformation of Maoping landslide after commission of Geheyan reservoir on the Qingjiang River, Hubei Province, China. *Eng. Geol*. **2006**, *86*, 37–51. https://doi.org/10.1016/j.enggeo.2006.04.004.
9. Huang, D.; Luo, S.L.; Zhong, Z.; Gu, D.M.; Song, Y.X.; Tomásd, R. Analysis and modeling of the combined effects of hydrological factors on a reservoir bank slope in the Three Gorges Reservoir area, China. *Eng. Geol*. **2020**, *279*, 105858. https://doi.org/10.1016/j.enggeo.2020.105858.
10. Luo, S.L.; Huang, D. Deformation characteristics and reactivation mechanisms of the Outang ancient landslide in the Three Gorges Reservoir, China. *Bull. Eng. Geol. Environ*. **2020**, *79*, 3943–3958. https://doi.org/10.1007/s10064-020-01838-3.
11. Luo, S.L.; Huang, D.; Peng, J.B.; Tomásd, R. Influence of permeability on the stability of dual-structure landslide with different deposit-bedding interface morphology: The case of the Three Gorges Reservoir area, China. *Eng. Geol*. **2022**, *296*, 106480. https://doi.org/10.1016/j.enggeo.2021.106480.
12. Yao, W.; Li, C.; Zuo, Q.; Zhan, H.; Criss, R.E. Spatiotemporal deformation characteristics and triggering factors of Baijiabao landslide in Three Gorges Reservoir region, China. *Geomorphology* **2019**, *343*, 34–47. https://doi.org/10.1016/j.geomorph.2019.06.024.
13. Shi, X.; Hu, X.; Sitar, N.; Kayen, R.; Qi, S.; Jiang, H.; Wang, X.; Zhang, L. Hydrological control shift from river level to rainfall in the reactivated Guobu slope besides the Laxiwa hydropower station in China. *Remote Sens. Environ*. **2021**, *265*, 112664. https://doi.org/10.1016/j.rse.2021.112664.
14. Ye, X.; Zhu, H.H.; Chang, F.N.; Xie, T.C.; Tian, F.; Zhang, W.; Catani, F. Revisiting spatiotemporal evolution process and mechanism of a giant reservoir landslide during weather extremes. *Eng. Geol.* **2024**, *332*, 107480. https://doi.org/10.1016/j.enggeo.2024.107480.
15. Alonso, E.E.; Pinyol, N.M. Criteria for rapid sliding I. A review of Vaiont case. *Eng. Geol*. **2010**, *114*, 198–210. https://doi.org/10.1016/j.enggeo.2010.04.018.
16. Kaczmarek, H.; Tyszkowski, S.; Banach, M. Landslide development at the shores of a dam reservoir (Włocławek, Poland), based on 40 years of research. *Environ. Earth Sci*. **2015**, *74*, 4247–4259. https://doi.org/10.1007/s12665-015-4479-3.
17. Chen, M.L.; Yang, X.; Zhou, J. Spatial distribution and failure mechanism of water-induced landslides in the reservoir areas of Southwest China. *J. Rock Mech. Geotech. Eng*. **2023**, *15*, 442–456. https://doi.org/10.1016/j.jrmge.2022.04.004.
18. Li, Q.P. Reservoir landslide of Huanglongtan Hydropower Station. *Hydroelectr. Power Generation*. **1989**, *1*, 35–39. (In Chinese)
19. Riemer, W. Landslides and reservoirs. In *Proceedings of the 6th International Symposium on Landslides*; Bell, D.H., Ed.; A.A. Balkema: Rotterdam, The Netherlands, 1992; pp. 1973–2004.
20. Yin, Y.P.; Huang, B.L.; Wang, W.P.; Wei, Y.J.; Ma, X.H.; Ma, F.; Zhao, C.J. Reservoir-induced landslides and risk control in Three Gorges Project on Yangtze River, China. *J. Rock Mech. Geotech. Eng*. **2016**, *8*, 577–595. https://doi.org/10.1016/j.jrmge.2016.08.001.
21. Li, S.; Xu, Q.; Tang, M.; Iqbal, J.; Liu, J.; Zhu, X.; Liu, F.; Zhu, D. Characterizing the spatial distribution and fundamental controls of landslides in the Three Gorges Reservoir, China. *B. Eng. Geol. Environ.* **2019**, *78*, 4275–4290. http://doi.org/10.1007/s10064-018-1404-5.
22. Qi, S.W.; Li, Y.C.; Liu, C.L.; Guo, X.Y.; Tang, F.J.; Lu, X.; Li, L.H.; Yang, G.X.; Sha, P.; Zhou, H.F.; et al. Risk of disturbance disasters of hydropower project in Hengduan Mountains. *Chin. J. Eng. Geol*. **2024**, *32*, 729–759. https://doi.org/10.13544/j.cnki.jeg.2024-0106. (In Chinese with English Abstract)
23. Behling, R.; Roessner, S.; Golovko, D.; Kleinschmit, B. Derivation of long-term spatiotemporal landslide activity—A multi-sensor time series approach. *Remote. Sens. Environ*. **2016**, *186*, 88–104. https://doi.org/10.1016/j.rse.2016.07.017.
24. Yang, X.; Chen, L. Using multi-temporal remote sensor imagery to detect earthquake-triggered landslides. *Int. J. Appl. Earth Obs. Geoinf*. **2010**, *12*, 487–495. https://doi.org/10.1016/j.jag.2010.05.006.
25. Đurić, D.; Mladenović, A.; Pešić-Georgiadis, M.; Marjanović, M.; Abolmasov, B. Using multiresolution and multitemporal satellite data for post-disaster landslide inventory in the Republic of Serbia. *Landslides* **2017**, *14*, 1467–1482. https://doi.org/10.1007/s10346-017-0847-2.
26. Guzzetti, F.; Mondini, A.C.; Cardinali, M.; Fiorucci, F.; Santangelo, M.; Chang, K.T. Landslide inventory maps: New tools for an old problem. *Earth Sci. Rev*. **2012**, *112*, 42–66. https://doi.org/10.1016/j.earscirev.2012.02.001.
27. Haneberg, W.C.; Cole, W.F.; Kasali, G. High-resolution lidar-based landslide hazard mapping and modeling, UCSF Parnassus Campus, San Francisco, USA. *Bull. Eng. Geol. Environ*. **2009**, *68*, 263–276. https://doi.org/10.1007/s10064-009-0204-3.
28. Kasai, M.; Ikeda, M.; Asahina, T.; Fujisawa, K. LiDAR-derived DEM evaluation of deep-seated landslides in a steep and rocky region of Japan. *Geomorphology* **2009**, *113*, 57–69. https://doi.org/10.1016/j.geomorph.2009.06.004.

29. Dun, J.; Feng, W.; Yi, X.; Zhang, G.; Wu, M. Detection and mapping of active landslides before impoundment in the Baihetan Reservoir area (China) based on the time-series InSAR method. *Remote Sens*. **2021**, *13*, 3213. https://doi.org/10.3390/rs13163213.
30. Liu, X.; Zhao, C.; Zhang, Q.; Lu, Z.; Li, Z.; Yang, C.; Zhu, W.; Liu-Zeng, J.; Chen, L.; Liu, C. Integration of Sentinel-1 and ALOS/PALSAR-2 SAR datasets for mapping active landslides along the Jinsha River corridor, China. *Eng. Geol*. **2021**, *284*, 106033. https://doi.org/10.1016/j.enggeo.2021.106033.
31. Zhao, C.; Kang, Y.; Zhang, Q.; Lu, Z.; Li, B. Landslide identification and monitoring along the Jinsha River Catchment (Wudongde Reservoir Area), China, using the InSAR method. *Remote Sens*. **2018**, *10*, 993. https://doi.org/10.3390/rs10070993.
32. Zhu, Y.; Yao, X.; Yao, L.; Zhou, Z.; Ren, K.; Li, L.; Yao, C.; Gu, Z. Identifying the mechanism of toppling deformation by InSAR: A case study in Xiluodu Reservoir, Jinsha River. *Landslides* **2022**, *19*, 2311–2327. https://doi.org/10.1007/s10346-022-01908-5.
33. Cook, M.E.; Brook, M.S.; Hamling, I.J.; Cave, M.; Tunnicliffe, J.F.; Holley, R. Investigating slow-moving shallow soil landslides using Sentinel-1 InSAR data in Gisborne, New Zealand. *Landslides* **2022**, *20*, 427–446. https://doi.org/10.1007/s10346-022-01982-9.
34. Shi, X.; Zhang, L.; Zhou, C.; Li, M.; Liao, M. Retrieval of time series three-dimensional landslide surface displacements from multi-angular SAR observations. *Landslides* **2018**, *15*, 1015–1027. https://doi.org/10.1007/s10346-018-0975-3.
35. Wasowski, J.; Bovenga, F. Investigating landslides and unstable slopes with satellite multi-temporal interferometry: Current issues and future perspectives. *Eng. Geol*. **2014**, *174*, 103–138. https://doi.org/10.1016/j.enggeo.2014.03.003.
36. Bishop, A.W. The Use of Slip Circle for the Stability Analysis of Slopes. *Geotechnique* **1955**, *5*, 7–17.
37. Zhang, P.Z.; Deng, Q.D.; Zhang, G.M.; Ma, J.; He, W.; Mao, F.Y.; Wang, Q. Active tectonic blocks and strong earthquakes in the continent of China. *Sci. China Ser. D Earth Sci.* **2003**, *46*, 13–24. https://doi.org/10.1360/zd2003-33-S1-12.
38. Qi, S.W. *Geological Structure Database of Qinghai Tibet Plateau*; National Tibetan Plateau/Third Pole Environment Data Center: Beijing, China, 2022. https://doi.org/10.11888/SolidEar.tpdc.272224.
39. Li, C.; Wang, X.; He, C.; Wu, X.; Kong, Z.; Li, X. National 1:200,000 Digital Geological Map (Public Version) Spatial Database (V1). Geological Development Research Center, China Geological Survey; China Geological Survey [Creating Institution], 1957. Available online: http://dcc.ngac.org.cn/geologicalData/rest/geologicalData/geologicalData-Detail/7d7ac63df9805f39a92591d105b7b0f2 (accessed on 30 January 2024).
40. Wen, X.Z.; Du, F.; Yi, G.X.; Long, F.; Fan, J.; Yang, P.X.; Xiong, R.W.; Liu, X.X.; Liu, Q. Earthquake potential of the Zhaotong and Lianfeng fault zones of the eastern Sichuan-Yunnan border region. *Chin. J. Geophys*. **2013**, *56*, 3361–3372. https://doi.org/10.6038/cjg20131012.
41. Zhang, M.; Ge, S.; Yang, Q.; Ma, X. Impoundment-associated hydro-mechanical changes and regional seismicity near the Xiluodu Reservoir, Southwestern China. *J. Geophys. Res. Sol. Ea*. **2021**, *126*, e2020JB021590. https://doi.org/10.1029/2020jb021590.
42. Peng, S. *1-km Monthly Precipitation Dataset for China (1901–2022)*; National Tibetan Plateau/Third Pole Environment Data Center: Beijing, China, 2020. https://doi.org/10.5281/zenodo.3185722.
43. Vinueza, A.U.; Handwerger, A.L.; Bakker, M.; Bogaard, T. A new method to detect changes in displacement rates of slow-moving landslides using InSAR time series. *Landslides* **2022**, *19*, 2233–2247. https://doi.org/10.1007/s10346-022-01913-8.
44. Li, L.; Wen, B.; Yao, X.; Zhou, Z.; Zhu, Y. InSAR-based method for monitoring the long-time evolutions and spatial-temporal distributions of unstable slopes with the impact of water-level fluctuation: A case study in the Xiluodu reservoir. *Remote Sens. Environ*. **2023**, *295*, 113686. https://doi.org/10.1016/j.rse.2023.113686.
45. Tang, C.; Tanyas, H.; van Westen, C.J.; Tang, C.; Fan, X.; Jetten, V.G. Analysing post-earthquake mass movement volume dynamics with multi-source DEMs. *Eng. Geol*. **2018**, *248*, 89–101. https://doi.org/10.1016/j.enggeo.2018.11.010.
46. Van den Bout, B.; Lombardo, L.; Chiyang, M.; van Westen, C.; Jetten, V. Physically-based catchment-scale prediction of slope failure volume and geometry. *Eng. Geol*. **2021**, *284*, 105942. https://doi.org/10.1016/j.enggeo.2020.105942.
47. Simonett, D.S. Landslide distribution and earthquakes in the Bewani and Torrecelli Mountains, New Guinea—A statistical analysis. In *Landform Studies from Australia and New Guinea*; Australian National University Press: Canberra, Australia, 1967; pp. 64–84.
48. Imaizumi, F.; Sidle, R.C. Linkage of sediment supply and transport processes in Miyagawa Dam catchment, Japan. *J. Geophys. Res. Atmos*. **2007**, *112*, 1–17. https://doi.org/10.1029/2006jf000495.
49. Guzzetti, F.; Ardizzone, F.; Cardinali, M.; Rossi, M.; Valigi, D. Landslide volumes and landslide mobilization rates in Umbria, central Italy. *Earth. Planet. Sci. Lett*. **2009**, *279*, 222–229. https://doi.org/10.1016/j.epsl.2009.01.005.
50. Larsen, I.J.; Montgomery, D.R.; Korup, O. Landslide erosion controlled by hillslope material. *Nat. Geosci*. **2010**, *3*, 247–251. https://doi.org/10.1038/ngeo776.

51. Guthrie, R.H.; Evans, S.G. Analysis of landslide frequencies and characteristics in a natural system, coastal British Columbia. *Earth Surf. Process. Landf.* **2004**, *29*, 1321–1339.
52. Brink, U.S.T.; Geist, E.L.; Andrews, B.D. Size distribution of submarine landslides and its implication to tsunami hazard in Puerto Rico. *Geophys. Res. Lett*. **2006**, *33*, 431–433. https://doi.org/10.1029/2006gl026125.
53. Tseng, C.; Lin, C.; Stark, C.P.; Liu, J.; Fei, L.; Hsieh, Y. Application of a multi-temporal, LiDAR-derived, digital terrain model in a landslide-volume estimation. *Earth Surf. Process. Landf*. **2013**, *38*, 1587–1601. https://doi.org/10.1002/esp.3454.
54. Ju, L.Y.; Zhang, L.M.; Xiao, T. Power laws for accurate determination of landslide volume based on high-resolution LiDAR data. *Eng. Geol*. **2022**, *312*, 106935. https://doi.org/10.1016/j.enggeo.2022.106935.
55. Yunus, A.P.; Xinyu, C.; Catani, F.; Subramaniam, S.S.; Fan, X.; Jie, D.; Sajinkumar, K.S.; Gupta, A.; Avtar, R. Earthquake-induced soil landslides: Volume estimates and uncertainties with the existing scaling exponents. *Sci. Rep*. **2023**, *13*, 8151. https://doi.org/10.1038/s41598-023-35088-6.
56. Malamud, B.D.; Turcotte, D.L.; Guzzetti, F.; Reichenbach, P. Landslide inventories and their statistical properties. *Earth. Surf. Proc. Land*. **2004**, *29*, 687–711. https://doi.org/10.1002/esp.1064.
57. Keefer, D.K. Statistical analysis of an earthquake-induced landslide distribution-the 1989 Loma Prieta, California event. *Eng. Geol.* **2000**, *58*, 231–249.
58. Li, L.; Yao, X.; Wen, B.; Zhou, Z.; Li, R. The long-term failure processes of a large reactivated landslide in the Xiluodu reservoir area based on InSAR technology. *Front. Earth Sci*. **2023**, *10*, 1055890. https://doi.org/10.3389/feart.2022.1055890.
59. Wei, J.; Wang, D.; Yang, Z.; Wang, J.; Li, Y.; Hu, W. Characteristics and mechanism of large deformation of a reservoir colluvial landslide—A case study of the Yulinerzu landslide in Xiluodu Reservoir, China. *Front. Earth Sci*. **2024**, *11*, 1337998. https://doi.org/10.3389/feart.2023.1337998.
60. Dafalla, M.A. Effects of clay and moisture content on direct shear tests for clay-sand mixtures. *Adv. Mater. Sci. Eng*. **2013**, *2013*, 562726. https://doi.org/10.1155/2013/562726.
61. He, C.; Hu, X.; Tannant, D.D.; Tan, F.; Zhang, Y.; Zhang, H. Response of a landslide to reservoir impoundment in model tests. *Eng. Geol*. **2018**, *247*, 84–93. https://doi.org/10.1016/j.enggeo.2018.10.021.
62. Li, S.; Sun, Q.; Zhang, Z.; Luo, X. Physical modelling and numerical analysis of slope instability subjected to reservoir impoundment of the Three Gorges. *Environ. Earth Sci*. **2018**, *77*, 138. https://doi.org/10.1007/s12665-018-7321-x.
63. Tang, M.; Xu, Q.; Yang, H.; Li, S.; Iqbal, J.; Fu, X.; Huang, X.; Cheng, W. Activity law and hydraulics mechanism of landslides with different sliding surface and permeability in the Three Gorges Reservoir Area, China. *Eng. Geol*. **2019**, *260*, 105212. https://doi.org/10.1016/j.enggeo.2019.105212.
64. Li, L.; Wen, B.; Yao, X.; Ren, K.; Zhu, Y. Deformation trends of two types of toppling in underdip and anti-dip bedding slopes under water-level fluctuations in the Xiluodu Reservoir using InSAR technology. *Landslides* **2024**, *21*, 697–716. https://doi.org/10.1007/s10346-023-02197-2.
65. Ren, K.; Li, R.; Yao, X.; Zhao, X.; Ma, L.; Yao, C.; Jiang, S.; Gu, Z.; Zhou, Z. Monitoring Yanwan deep-seated toppling deformation with the impact of water-level fluctuation by SAR observations. *Landslides* **2024**, *21*, 1243–1254. https://doi.org/10.1007/s10346-024-02220-0.
66. Li, D.; Yin, K.; Leo, C. Analysis of Baishuihe landslide influenced by the effects of reservoir water and rainfall. *Environ. Earth Sci*. **2010**, *60*, 677–687. https://doi.org/10.1007/s12665-009-0206-2.
67. Chen, M.L.; Qi, S.C.; Lv, P.F.; Yang, X.G.; Zhou, J.W. Hydraulic response and stability of a reservoir slope with landslide potential under the combined effect of rainfall and water level fluctuation. *Environ. Earth Sci*. **2021**, *80*, 25. https://doi.org/10.1007/s12665-020-09279-7.
68. Jia, G.W.; Zhan, T.L.T.; Chen, Y.M.; Fredlund, D.G. Performance of a large-scale slope model subjected to rising and lowering water levels. *Eng. Geol*. **2009**, *106*, 92–103. https://doi.org/10.1016/j.enggeo.2009.03.003.
69. Xia, M.; Ren, G.M.; Zhu, S.S.; Lei, X. Relationship between landslide stability and reservoir water level variation. *Bull. Eng. Geol. Environ*. **2014**, *74*, 909–917. https://doi.org/10.1007/s10064-014-0654-0.
70. Alonso, E.E.; Pinyol, N.M. Numerical analysis of rapid drawdown: Applications in real cases. *Water. Sci. Eng*. **2016**, *9*, 175–182. https://doi.org/10.1016/j.wse.2016.11.003.
71. Wu, Z.; Xie, M.; Zhang, X.; Lu, G.; Zhao, C.; Zhang, X. Model test study on natural frequency evolution and early warning of reservoir landslides under water level fluctuations. *Nat. Hazards* **2024**, *120*, 6881–6900. https://doi.org/10.1007/s11069-024-06475-7.

72. Xiong, X.; Shi, Z.; Xiong, Y.; Peng, M.; Ma, X.; Zhang, F. Unsaturated slope stability around the Three Gorges Reservoir under various combinations of rainfall and water level fluctuation. *Eng. Geol*. **2019**, *261*, 105231. https://doi.org/10.1016/j.enggeo.2019.105231.
73. Zhang, W.; Meng, X.; Wang, L.; Meng, F. Stability analysis of the reservoir bank landslide with weak interlayer considering the influence of multiple factors. Geomatics. *Nat. Hazards Risk*. **2022**, *13*, 2911–2924. https://doi.org/10.1080/19475705.2022.2149356.
74. Huang, D.; Gu, D.M.; Song, Y.X.; Cen, D.F.; Zeng, B. Towards a complete understanding of the triggering mechanism of a large reactivated landslide in the Three Gorges Reservoir. *Eng. Geol*. **2018**, *238*, 36–51. https://doi.org/10.1016/j.enggeo.2018.03.008.
75. Yang, H.; Jian, W.; Wang, F.; Meng, F.; Okeke, A.C. Numerical simulation of failure process of the Qianjiangping landslide triggered by water level rise and rainfall in the Three Gorges Reservoir, China. In *Progress of Geo-Disaster Mitigation Technology in Asia*; Springer: Berlin/Heidelberg, Germany, 2012; pp. 503–523. https://doi.org/10.1007/978-3-642-29107-4_29.
76. Fan, L.; Lehmann, P.; Zheng, C.; Or, D. Rainfall intensity temporal patterns affect shallow landslide triggering and hazard evolution. *Geophys. Res. Lett*. **2019**, *47*, e2019GL085994. https://doi.org/10.1029/2019gl085994.
77. Ye, X.; Zhu, H.; Wang, J.; Zhang, Q.; Shi, B.; Schenato, L.; Pasuto, A. Subsurface multi-physical monitoring of a reservoir landslide with the fiber-optic nerve system. *Geophys. Res. Lett*. **2022**, *49*, e2022GL098211. https://doi.org/10.1029/2022gl098211.
78. Xia, M.; Ren, G.M.; Lei, X. Deformation and mechanism of landslide influenced by the effects of reservoir water and rainfall, Three Gorges, China. *Nat. Hazards*. **2013**, *68*, 467–482. https://doi.org/10.1007/s11069-013-0634-x.
79. Westra, S.; Fowler, H.J.; Evans, J.P.; Alexander, L.V.; Berg, P.; Johnson, F.; Kendon, E.J.; Lenderink, G.; Roberts, N.M. Future changes to the intensity and frequency of short-duration extreme rainfall. *Rev. Geophys*. **2014**, *52*, 522–555. https://doi.org/10.1002/2014rg000464.
80. Yuan, Z.; Yin, J.; Wei, M.; Yuan, Y. Spatio-Temporal Variations in the Temperature and Precipitation Extremes in Yangtze River Basin, China during 1961–2020. *Atmosphere* **2021**, *12*, 1423. https://doi.org/10.3390/atmos12111423.
81. Guo, X.; Fu, B.; Du, J.; Shi, P.; Li, J.; Li, Z.; Du, J.; Chen, Q.; Fu, H. Monitoring and Assessment for the Susceptibility of Landslide Changes After the 2017 Ms 7.0 Jiuzhaigou Earthquake Using the Remote Sensing Technology. *Front. Earth Sci.* **2021**, *9*, 633117. https://doi.org/10.3389/feart.2021.633117.
82. Behling, R.; Roessner, S. Spatiotemporal Landslide Mapper for Large Areas Using Optical Satellite Time Series Data. In *Advancing Culture of Living with Landslides*; Springer International Publishing: Berlin/Heidelberg, Germany, 2017; pp. 143–152. https://doi.org/10.1007/978-3-319-53498-5_17.
83. Martha, T.R.; Kerle, N.; van Westen, C.J.; Jetten, V.; Vinod Kumar, K. Object-oriented analysis of multi-temporal panchromatic images for creation of historical landslide inventories. *ISPRS J. Photogramm. Remote Sens.* **2012**, *67*, 105–119. https://doi.org/10.1016/j.isprsjprs.2011.11.004.
84. Ghorbanzadeh, O.; Gholamnia, K.; Ghamisi, P. The application of ResU-net and OBIA for landslide detection from multi-temporal Sentinel-2 images. *Big Earth Data* **2022**, *7*, 961–985. https://doi.org/10.1080/20964471.2022.2031544.